JOURNAL OF GEOPHYSICAL RESEARCH, VOL. 100, NO. C4, PAGES 6845–6863, APRIL 15, 1995

Wind and thermohaline circulation of the Black Sea driven by yearly mean climatological forcing

T. Oguz[1]

Department of Earth, Atmospheric and Planetary Sciences, Massachusetts Institute of Technology Cambridge
Department of Geology and Geophysics, Woods Hole Oceanographic Institution, Woods Hole Massachusetts

P. Malanotte-Rizzoli

Department of Earth, Atmospheric and Planetary Sciences, Massachusetts Institute of Technology Cambridge

D. Aubrey

Department of Geology and Geophysics, Woods Hole Oceanographic Institution, Woods Hole Massachusetts

Abstract. Using an eddy-resolving ocean circulation model endowed with active thermodynamics and a turbulence closure parameterization, a hierarchy of numerical experiments is carried out to investigate the relative contributions of the wind forcing, the surface thermohaline fluxes, the river runoff, and the Bosphorus inflow/outflow in driving the yearly mean circulation in the Black Sea. The model accommodates a topographic and boundary-fitted curvilinear coordinate system and resolves steep topographical changes around the periphery of the basin using $O(10$ km) grid spacing and 18 stretched vertical levels. Model experiments show that topography, wind forcing, and buoyancy forcing are all first-order contributors to the primary circulation of the Black Sea. If any of these features are neglected, significant elements of the model circulation do not reproduce observations. Subbasin scale gyres are caused by both wind and thermohaline forcing. Annual mean wind stress is sufficient to produce the major interior cyclonic gyres. Stronger winds produce more defined interior flow than the weaker winds of the Hellermann and Rosenstein (1983) fields. Heat flux is an important contributor to subbasin scale cyclonic circulation. However, the annual mean heat flux with spatial structure given by the climatology produces unrealistic features in the interior circulation. The latter ones disappear when including the seasonal heat flux variability. This results strongly suggests that the seasonal cycle of the wind stress is much less crucial than the heat flux seasonal cycle in producing a realistic basin circulation. The Rim Current is locked to the steep topographic shelf slope, regardless of the forcing mechanism. Without including the strong topography the Rim Current is absent for all forcings. Mesoscale variability arises from the dynamic evolution of the Rim Current. This variability is enhanced by the Danube inflow and the Bosphorus inflow/outflow, demonstrating the importance of these buoyancy sources in enhancing the mesoscale. The deep-layer circulation is controlled by the barotropic pressure gradient and is insensitive to the magnitude, seasonality, or strength of the surface forcing. A transition zone separates the surface and deep-layer circulation patterns. Its circulation is mainly driven by the slope of the pycnocline developed as a response to the surface forcing.

1. Introduction

The Black Sea, located between latitudes of 41° to 46°N and longitudes of 28° to 41.5°E, is an anoxic marginal sea having limited interaction with the Mediterranean and Azov Seas through the Turkish straits system and the Kerch Strait, respectively. It is an elongated, elliptic-shaped basin distorted by the Crimean peninsula on the north and the curvature of the Turkish coastline on the south. A large triangular shelf region, constituting about 20% of the area of whole sea, covers the northwest part. From here the shelf gradually narrows toward the southwest and terminates to the east of the Bosphorus. Only the upper 100 to 150 m of the total 2200-m water depth possesses measurable oxygen; the rest of the water mass is anoxic.

The Black Sea is intrinsically interesting to oceanographers for numerous scientific reasons. First, it is a nearly enclosed marginal sea, small enough to be logistically easily

[1]Permanently at Institute of Marine Sciences, Middle East Technical University, Icel, Turkey.

Paper number 95JC00022.
0148-0227/95/95JC-00022$05.00

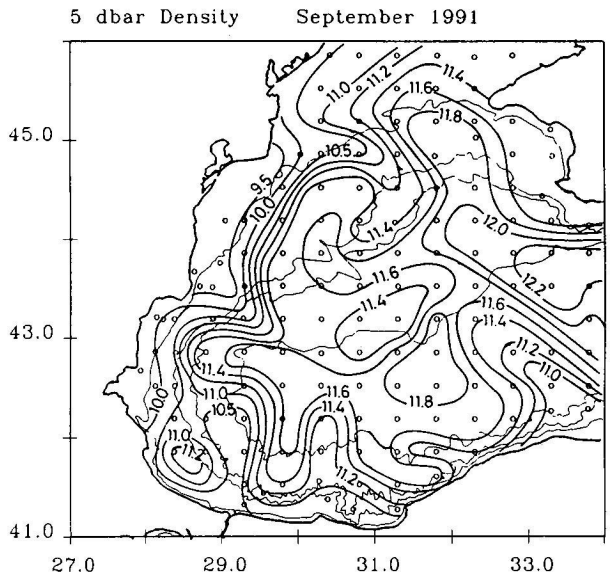

Figure 1. The 5-dbar density distribution in the western Black Sea during September 1991.

accessible but large enough for the circulation to obey vorticity dynamics. In it, important processes occur, such as water mass formation, that are common to major oceanic basins, but can be much more easily studied observationally. Notable features of this basin include the lack of open boundaries and the equal importance of the wind stress field and surface thermohaline fluxes in driving the complex flow system. The circulation is modified regionally by inflow/outflow from the straits and freshwater discharges from major rivers on the continental shelf. A bottom relief characterized by steep slopes exerts an important control on the circulation.

The Black Sea is a dilution basin with a positive water balance resulting from excess precipitation (~300 km^3/yr) and runoff (~350 km^3/yr) over evaporation (~353 km^3/yr). A surface flow of ~610 km^3/yr of less saline (~18 parts per thousand (ppt)) and lighter water exits from the Black Sea into the Aegean Sea. In return the saltier (>22 ppt) and denser Mediterranean water of ~313 km^3/yr flows into the Black Sea as an underflow. The continuous influx of saline water from the Turkish straits maintains the salinity of intermediate and deep water masses of the Black Sea at a constant value, resulting in the formation of a permanent halocline at depths of 100–150 m. This two-layer hydrological structure has evolved within the last 7000–9000 years, after the Black Sea established connection with the Mediterranean Sea [*Boudreau and Leblond*, 1989].

The volume fluxes given above are based on two-layer budget calculations of the coupled system comprising the Turkish straits and the Black Sea [*Unluata et al.*, 1989]. The general TS characteristics of the Black Sea are described by *Murray et al.* [1991] and *Oguz et al.* [1992, 1993, 1994]. A review of the oceanography of the northwestern shelf is given by *Tolmazin* [1985a]. Observational studies of the mixing, spreading, and sinking characteristics of the dense Mediterranean underflow are reported by *Tolmazin* [1985b], *Yuce* [1990], *Latif et al.* [1991], *Oguz and Rozman* [1991], and *Ozsoy et al.* [1993]. Studies on the biogeochemistry of the sea, in general, and of the oxic/anoxic interface zone, in particular, are presented in a series of papers by *Murray* [1991] and *Izdar and Murray* [1992].

The freshwater discharge into the northwest shelf is crucial in making the sea a dilution basin. The major outflows are from the following three rivers: the Danube, the Dniepr, and the Dniestr. The Danube provides the major input of fresh water (~250 km^3/yr), influencing the circulation, mixing properties, and the entire ecosystem of the shelf region. The Danube plume forms an anticyclonic bulge confined within the upper 25-m layer. The leading edge of this plume protrudes southward (i.e., downstream) as a thin baroclinic boundary current along the western coastline. The coastal jet is separated from the interior waters by a well-defined salinity front (Figure 1).

Wintertime cooling is another important process leading to cold water formation and subsequent regeneration and replenishment of the Cold Intermediate Layer (CIL) [*Filippov*, 1965; *Tolmazin*, 1985a; *Ovchinnikov and Popov*, 1987]. The relative importance of these processes in driving both the shelf and the interior circulations is not yet understood. Also not understood are the interaction mechanisms between the interior and the shelf flows.

The Black Sea is characterized by a predominantly cyclonic basin-wide circulation. The building blocks of the general circulation (Figure 2a) are the Rim Current flowing along the abruptly varying continental slope and margin topography all around the basin, a multicentered cyclonic cell occupying the interior of the sea, and a series of anticyclonic eddies confined inshore of the Rim Current [*Oguz et al.*, 1993; *Eremeev et al.*, 1992]. This pattern, providing an improvement to the classical twin-gyre cyclonic circulation concept, is further revised by the recent findings of the Cooperative Marine Science Program for the Black Sea (CoMSBlack) hydrographic surveys [*Oguz et al.*, 1994, 1995] and satellite imagery [*Sur et al.*, 1995]. The new findings reveal a complex, eddy-dominated circulation. The Rim Current exhibits large meanders, offshore filaments, and dipole eddy structure (Figure 2b). The interior circulation is composed of an interconnecting series of cyclonic eddies and subbasin scale gyres, varying in size and shape across the basin and with depth. They evolve continuously by interactions among each other, as well as with the Rim Current. The circulation is strongest in the upper layer, where the geostrophic currents have speeds of typically 25 cm/s along the axis of the Rim Current (Figure 2b). Recent acoustic Doppler current profiler (ADCP) measurements [*Oguz et al.*, 1995], on the other hand, indicated stronger Rim Current structure, typically >50 cm/s within the upper layer and ~20 cm/s within the 200- to 400-m depth range.

Contrary to the upper layer circulation, knowledge of the flow field below ~300 m is limited and generally unreliable. Recent hydrographic observations [*Oguz et al.*, 1993, 1994] indicate considerable structural variability of the circulation at depths below 300 m.

Modeling efforts of the Black Sea circulation have been rather limited. A common feature of the majority of existing models is their coarse horizontal resolution and relatively strong dissipation necessary for numerical stability. The models thus do not resolve the mesoscale eddy field and can only reproduce the coarse, large-scale features of the general circulation in response to the seasonal wind and thermohaline forcing.

The most simplistic and earliest models are based on

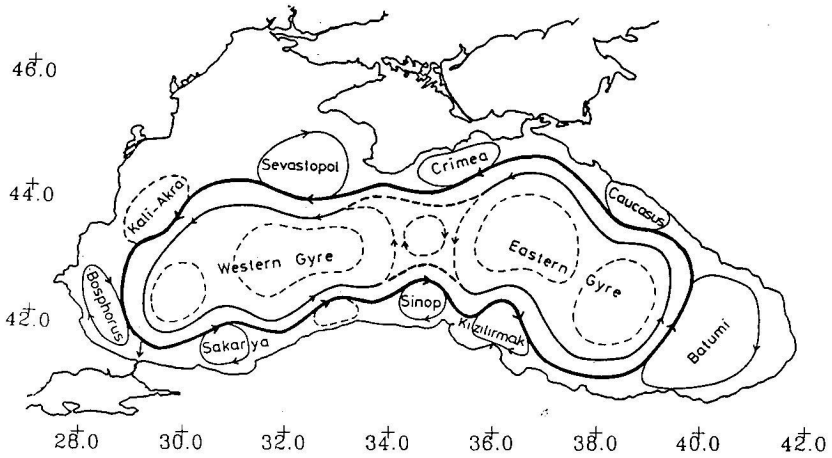

Figure 2a. Schematic diagram of the upper layer circulation in the Black Sea. Reprinted from *Oguz et al.* [1993], with kind permission from Elsevier Science Ltd., The Boulevard, Langford Lane, Kidlington OX5 1GB, United Kingdom.

Sarkisyan's diagnostic modeling approach [*Dzhioev and Sarkisyan*, 1976; *Gamsakhurdiya and Sarkisyan*, 1976; *Moskalenko*, 1976]. These models noted the importance of the "jebar" effect in driving the wind-driven circulation. The interannual variability of currents in the Black Sea has been studied more recently using "semidiagnostic" models [*Stanev et al.*, 1988; *Eremeev et al.*, 1992; *Demyshev*, 1992; *Trukhchev and Demin*, 1992; *Klimok and Makeshov*, 1993]. The success of these models in predicting mesoscale features of the circulation has been limited by the resolution of the climatological data. With coarse resolution (typically 40 × 60 arc min) data sets, smoothed circulation patterns were obtained consisting of only the largest-scale features. When the climatological fields were interpolated on a finer grid (e.g., 21 × 28 arc min), some smaller-scale features of the general circulation were reproduced. These efforts focused mostly on the wind-driven component of the circulation. The role of buoyancy fluxes to the generation of upper layer currents comparable to those generated by the wind stress was noted by *Marchuk et al.* [1975], *Stanev* [1990], and S. N. Bulgakov et al. (unpublished manuscript, 1995).

Using a fully eddy-resolving ocean circulation model, we carry out a systematic series of numerical experiments to address the following fundamental questions: (1) what is the relative importance of the wind stress, air-sea thermohaline fluxes, and lateral buoyancy fluxes in driving the general circulation on the yearly timescale; (2) what is the spatial variability of the general circulation due to the regional variability of these forcing agents; and (3) how is the yearly general circulation modulated by the mesoscale variability generated by the currents in response to the internal dynamical processes.

Sections 2 and 3 present the model formulation and initial and boundary conditions, respectively. The results of the numerical experiments designed to study the effect of each forcing mechanism are given in section 4. A summary and discussion of these results are provided in section 5, as well as the directions for future research.

2. Model Description

The model implemented for this study is the Princeton ocean model (POM) described by *Blumberg and Mellor* [1987] and *Blumberg and Herring* [1987]. It is a free-surface

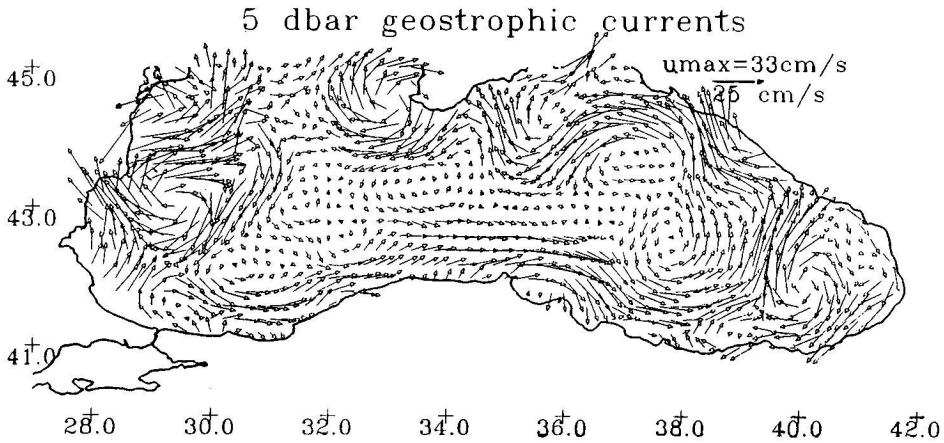

Figure 2b. The 5-dbar geostrophic circulation during September 1991. Reprinted from *Oguz et al.* [1994], with kind permission from Elsevier Science Ltd., The Boulevard, Langford Lane, Kidlington OX5 1GB, United Kingdom.

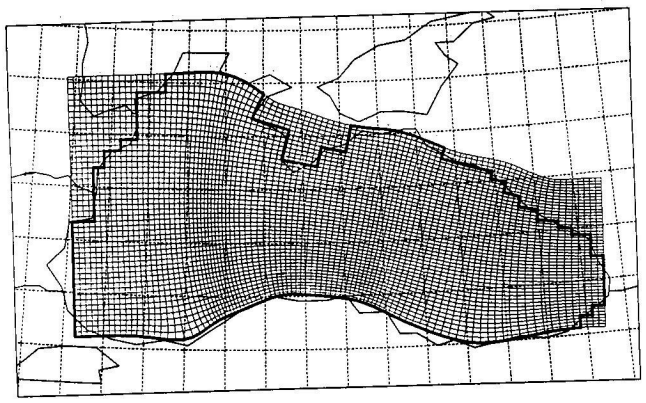

Figure 3. Model curvilinear grid.

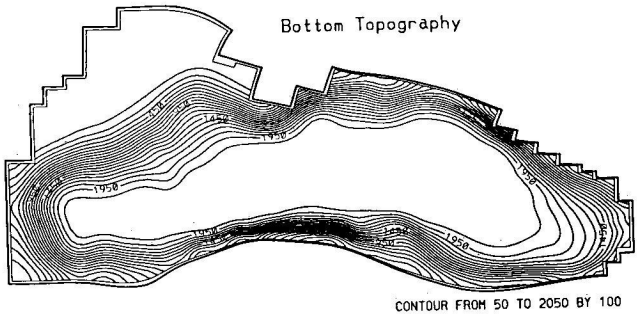

Figure 4. Smoothed model topography (depths are in meters).

primitive equation model for an incompressible, Boussinesq, and hydrostatic fluid employing bottom-following σ coordinate in the vertical and a coast-following orthogonal curvilinear coordinate system in the horizontal. It incorporates active thermodynamics, and the Mellor-Yamada level 2.5 turbulence closure scheme [*Mellor and Yamada*, 1982] for the parameterization of vertical mixing. It has been applied to numerous oceanic problems including estuarine and shelf circulation studies [*Blumberg and Mellor*, 1983; *Oey et al.*, 1985], data assimilation studies in the Gulf Stream [*Mellor and Ezer*, 1991], and general circulation studies in the Mediterranean Sea [*Zavatarelli and Mellor*, 1995]. A brief description of the model and of the grid configuration, as well as a short summary of the numerical schemes used, described in detail by *Mellor* [1991], are given in the appendix.

The model domain covers the entire sea including the shallow northwestern and western shelf regions and is shown in Figure 3 with the curvilinear grid. It has a resolution of ~5 km along most of the southern coast, where the topography undergoes its most drastic variations. In the interior of the basin, where the topography is almost flat, the grid spacing increases maximally to ~15 km. The average grid spacings of ~8.5 and ~11.5 km in the meridional and zonal directions, respectively, are less than half the first baroclinic radius of deformation of 20–30 km.

Table 1. Position of σ Levels for Different Water Depths

Level	Position	100 m	500 m	2000 m
1	0.000	0.0	0.0	0.0
2	−0.004	−0.4	−2.2	−8.8
3	−0.007	−0.7	−3.4	−13.5
4	−0.010	−1.0	−5.2	−20.8
5	−0.016	−1.6	−8.0	−32.1
6	−0.025	−2.5	−12.4	−49.6
7	−0.038	−3.8	−19.1	−76.4
8	−0.059	−5.9	−29.5	−117.9
9	−0.091	−9.1	−45.4	−181.8
10	−0.140	−14.0	−70.1	−280.3
11	−0.167	−16.7	−83.3	−333.3
12	−0.333	−33.3	−166.7	−666.7
13	−0.500	−50.0	−250.0	−1000.0
14	−0.667	−66.7	−333.3	−1333.3
15	−0.827	−82.7	−413.3	−1653.1
16	−0.910	−91.0	−454.9	−1819.5
17	−0.953	−95.3	−476.5	−1906.0
18	−1.000	−100.0	−500.0	−2000.0

Eighteen vertical levels are used. These levels are stretched exponentially toward the free surface to achieve a better resolution of the upper layer stratification. Accordingly, the upper 200-m layer, where the density changes are about 4–5 kg/m^3 (see Figure 6), is resolved by at least nine vertical levels. This resolution becomes finer as the water depth becomes shallower (Table 1).

3. Initial and Boundary Data

3.1. Bottom Topography

The bottom topography is interpolated to the model grid from the 5 × 5 arc min world ocean topographic data set. A fourth-order Shapiro filter is applied twice to smooth out steep topographic features which are expected to introduce some errors in the velocity and density fields due to the application of the σ coordinate system (see appendix). The resultant bathymetry (Figure 4) exhibits a narrow shelf O(50 km) and steep slope all around the basin. Toward the interior, this steep topographic slope joins an almost flat abyssal basin with a depth of ~2200 m. In the western basin the northwestern shelf region is coupled to the interior through a relatively wide and smooth topographic slope. The minimum depth of the shelf is set to 50 m.

3.2. Wind Stress

The yearly mean wind stress field is derived from the *Hellermann and Rosenstein* [1983] monthly climatologies. The eastward and northward components of the wind stress field are first interpolated onto the model grid and then rotated onto the curvilinear coordinate system. The field

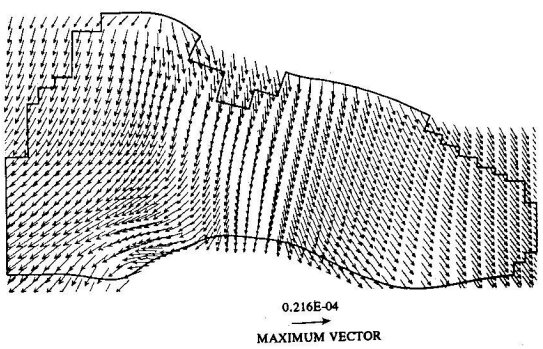

Figure 5. Climatological yearly mean *Hellermann and Rosenstein* [1983] wind stress field (in dynes per square centimeter).

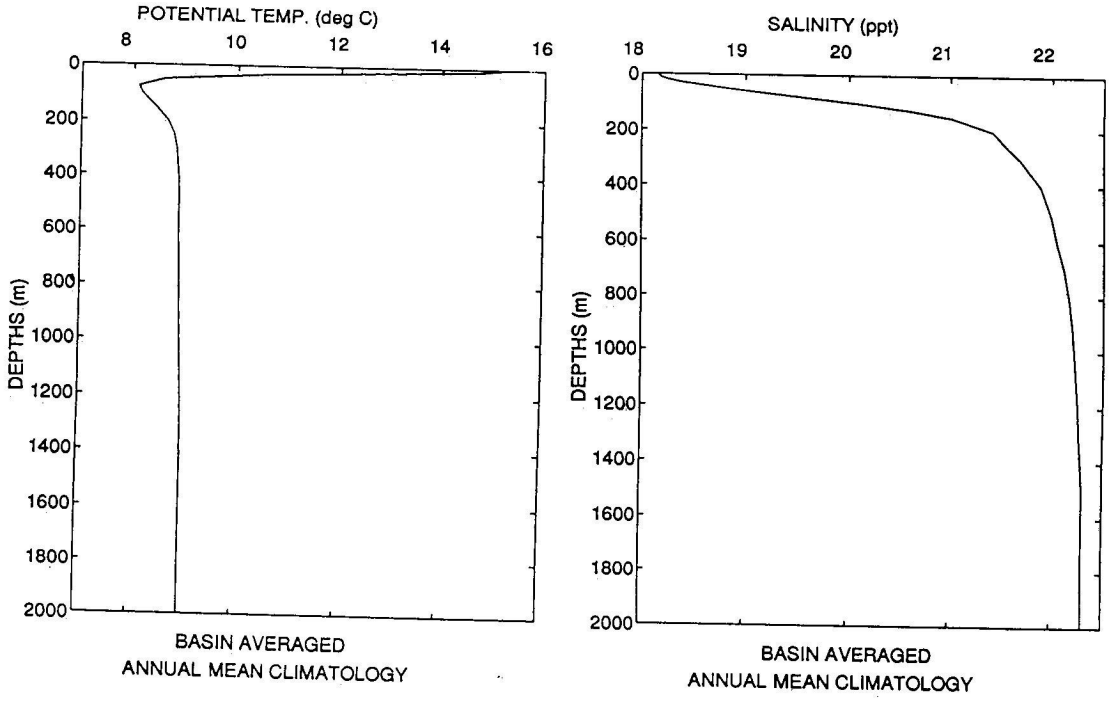

Figure 6. Climatological mean vertical (left) temperature and (right) salinity profiles used in the model initialization.

(Figure 5) is dominated by northerlies having a magnitude of <0.2 dyn/cm^2. The dominant direction of the winds is from the northeast, the north, and the northwest in the western, central, and eastern basins, respectively.

The *Hellermann and Rosenstein* [1983] climatology is a relatively weak and smoothed wind stress field. The directions are generally in agreement with those of other data sets used in different studies [e.g., *Stanev et al.*, 1995; S. P. Meacham, On the circulation of the Black Sea at the basin scale and the mesoscale, submitted to *Deep-Sea Research*, hereinafter referred to as submitted manuscript, 1994], but the magnitudes seem to be rather smaller, with a maximum intensity not exceeding 0.5 dyn/cm^2 throughout the climatological year. The curl of wind stress field has typical magnitudes of 10^{-10} dyn/cm^3, an order of magnitude smaller than the basin average value reported by *Stanev et al.* [1995]. Although the *Hellermann and Rosenstein* [1983] winds are known to be weak, these are used in this study because they are the best documented, available wind stress fields for this region.

3.3. Stratification

The annual mean temperature and salinity fields are reconstructed from the monthly fields based on the Russian climatology of ~25,000 conductivity-temperature-depth (CTD) and Nansen bottle casts collected within the last 70 years [*Altman et al.*, 1987]. The data were made available to us by I. Gertman and have a spatial resolution of 1° longitude and 0.5° latitude comprising 97 grid boxes over the entire sea. The data set consists of the monthly averages of temperature and salinity fields at 22 vertical levels.

In all experiments the model is initialized with horizontally uniform, one-dimensional stratification (Figure 6). The profiles are obtained by averaging their climatological fields horizontally at each standard depth level and then by interpolating to the sigma surfaces at each grid point. These mean profiles show the main observed stratification characteristics for most of the year, except during winter cold intermediate water formation. The upper layer consists of two distinct water masses. A thin (~25 m) surface layer is characterized by less saline (~18 ppt) and warm water. Below it the cold intermediate water mass is found, identified in this climatological profile by the temperature of ~8.0°C. At the depth of 200 m, corresponding to the base of the pycnocline, the mean values of temperature and salinity are 8.7°C, 21.4 ppt, corresponding to a density of 16.5 kg/m^3. The TS characteristics of the water masses in the lower layers are rather uniform. The mean temperature and salinity values of 8.9°C and 22.0 ppt at 500 m increase only to 9.0°C and 22.30 ppt at 1500 m, below which they remain constant within the convectively mixed bottom layer.

3.4. Surface Fluxes

The surface thermohaline fluxes are specified from the climatological maps of evaporation, precipitation, and total heat fluxes [*Simonov and Altman*, 1991]. The annual mean heat flux has a zonally uniform distribution but significant north-to-south variability. The northern parts of the basin are characterized by net heat loss to the atmosphere in excess of 50 W/m^2 along the Caucasian coast and to the west of the Crimean peninsula. The heat flux changes sign approximately at 43°N, and the southern basin gains heat from the atmosphere, with a maximum mean value of ~30 W/m^2 along the Turkish coast. When integrated over the basin, there is a net excess of 7.7 W/m^2 annual heat influx into the sea. Since the experiments driven by surface flux alone (section 4.2) are carried out in the closed basin configuration, the basin-integrated heat flux is made zero by subtracting this excess heat flux uniformly from the warming part of the

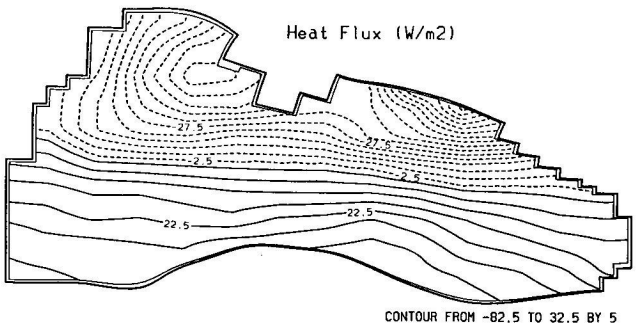

Figure 7a. Yearly mean climatological heat flux distribution (in watts per square meter).

basin. The resulting "modified" heat flux distribution is similar to the original one (Figure 7a).

The climatological data yield a total annual evaporation of 384 km^3/yr and a precipitation rate of 227 km^3/yr. The precipitation is generally greater along the Turkish and Caucasian coast (~700–1000 mm/yr), with maximum values of ~2000 mm/yr near the southeastern end of the basin. It decreases diagonally toward the northwestern shallow part of the basin where it attains its lowest values of ~250 mm/yr. The evaporation tends to have an almost opposite spatial distribution, with values in excess of 1000 mm/yr in the northern-northwestern sector decreasing to ~750 mm/yr near the southeastern corner where the precipitation has its maximum intensity. Therefore the evaporation (E) and precipitation (P) rates are comparable over most of the basin, and the E minus P (E − P) distribution has distinct regional characteristics. Generally, it is dominated by the excess of evaporation for most of the sea. It decreases gradually toward the south and the central part of the eastern basin and then changes sign, implying excess of precipitation near the southeastern corner. Considering the basin to be completely closed with no additional source/sink of freshwater flux, the excess of the basin-integrated evaporation (384 − 227 = 157 km^3/yr) is removed uniformly from the evaporation distribution. The total annual evaporation is thus reduced to 227 km^3/yr which leads to zero net E − P flux within the basin. The resulting modified distribution of E − P, given in terms of millimeters per day (Figure 7b), is similar to the original one.

3.5. Lateral Fluxes

A total transport of 10,000 $m^3\ s^{-1}$ is prescribed as the total freshwater input into the basin at two grid points approximating the Danube estuary. Smaller contributions of Dniepr and Dniestr Rivers (<3000 $m^3\ s^{-1}$) are thus combined with the Danube forcing, which has a long-term average value of ~7000 $m^3\ s^{-1}$. Since the three river estuaries are indeed quite near one another, the response of the circulation would be substantially the same if these local sources were separated. The important quantity is the total volume of freshwater outflow over the shelf.

The temperature and salinity of the inflow are kept fixed in time and assumed to be vertically uniform with values of S_0 = 5.0 ppt and T_0 = 13.0°C. The temperature of the inflow is thus similar to the ambient conditions, whereas the salinity is much lower. The inflow may therefore be traced by the low salinity of the discharge inside the basin.

Imposing a Danube influx also requires opening the Bosphorus Strait to balance the freshwater inflow with the outflow from the strait. The Bosphorus Strait is modeled as a two grid point opening where the climatological profiles prescribed initially are similar to those shown in Figure 6, except that they are set to the boundary values of S_B = 23 ppt and T_B = 12°C within the last 10 m depth of the 50-m thick water column. During the model integration the boundary values of the temperature and salinity are determined according to the direction of the flow (see appendix). Thus, in addition to the Danube inflow, the model incorporates inflow of dense Mediterranean underflow into the sea at the Bosphorus.

4. Results of Numerical Experiments

An extensive series of numerical experiments has been carried out to study systematically the response of the circulation to each of the three forcing mechanisms (wind stress, surface thermohaline fluxes, and river runoff and Bosphorus inflow/outflow), first in isolation from each other and then in various combinations. Table 2 summarizes the numerical experiments we describe here. In Table 2 the experiment numbers, shown in the first column, are followed by columns showing the types of forcing used in each experiment. The last three columns provide information on the type of topography, stratification, and geometry used.

Experiments 1 to 3 investigate the purely wind-driven circulation, with or without topography in the barotropic (experiment 1) and baroclinic oceans (experiment 2 and 3). Experiments 4 and 5 investigate the roles first of the precipitation and evaporation fluxes alone (experiment 4), then together with the total heat flux (experiment 5). Experiments 4 and 5 are motivated by the fact that the annual mean thermohaline fluxes (Figures 7a and b) reveal distinct spatial structural variability. We wish to find out how this variability is reflected by the annual mean circulation of the Black Sea. All of these experiments are carried out with a closed geometry. In experiment 6, on the other hand, we consider the large-scale circulation driven only by coastal freshwater discharge and the source/sink flow through the Bosphorus Strait. Therefore we switch off both the wind and surface thermohaline forcings and consider only the volume and buoyancy fluxes from a point source along the coast. We also replace the stair-step representation of the coastal wall in the vicinity of the freshwater source with a smoother coastal configuration to avoid the noisiness, numerically

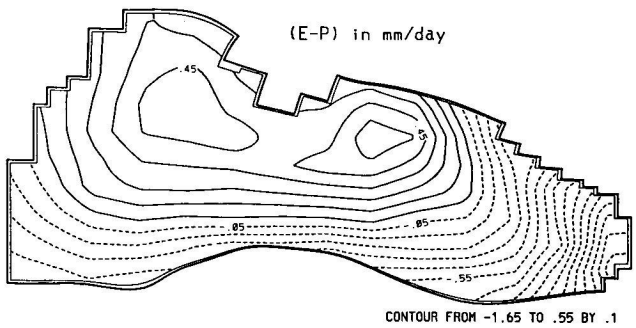

Figure 7b. Yearly mean climatological evaporation minus precipitation (E − P) distribution (millimeters per day).

Table 2. List of Numerical Experiments

Experiment	Types of Forcing				Topography	Stratification	Geometry
	Wind	Thermal	Salt	Runoff			
1	on	off	off	off	on	off	C
2	on	off	off	off	off	on	C
3	on	off	off	off	on	on	C
4	off	off	E − P	off	on	on	C
5	off	Q	E − P	off	on	on	C
6	off	off	off	on	on	on	O
7	on	Q	E − P	on	on	on	O
8a	on	Q	E − P	off	on	on	C
8b	on*	Q	E − P	off	on	on	C
8c	on	$Q(t)$	E − P	off	on	on	C

On indicates forcing is on; off indicates forcing is off. E − P is the yearly mean evaporation minus precipitation rate, Q is the yearly mean total heat flux, and $Q(t)$ is the seasonally varying but horizontally homogeneous total heat flux. C denotes the basin is closed, O denotes it is open.

*Stronger wind stress forcing is present.

generated in the vicinity of stair-step corners during spin-up (Figure 13). Experiments 7 and 8a–8c have multiple forcings. We refer to experiment 7 as the "central experiment" which describes the annual mean circulation driven by all the three major driving mechanisms. The central experiment is complemented by three additional experiments (experiments 8a–8c) which investigate the response of the sea to different combinations of the wind stress and surface fluxes in a closed geometry.

Starting from an initial state of rest, the model is integrated until statistically steady state is reached. The time evolution of the solution is examined by monitoring the total kinetic energy, as well as some other basin-integrated quantities. The spin-up timescale is generally short, on the order of 1–2 years, depending on the experiments. The time integration, however, is continued at least for another year after spin-up. Analysis of the model results is based on the daily mean fields to remove all high-frequency variability introduced by the free-surface and internal gravity waves.

Some experiments were initially carried out to test the performance of the model and to assess its sensitivity to some model parameters. The overall, basin-wide circulation is not affected by the planetary beta, as the Black Sea is a zonal channel with relatively small north-south extension. However, in all the experiments the actual latitude-dependent Coriolis parameter was retained as the mesoscale activity, and the Rim Current meandering and instabilities are governed by vorticity dynamics; hence on the eddy scale the beta effect is important. The horizontal eddy viscosity and diffusivity are taken as 100 m^2/s values or calculated by the Smagorinsky formulation. For values <100 m^2/s, either constant or calculated by the Smagorinsky formulation, the circulation is not sensitive to their choice. The vertical eddy coefficients are computed by the *Mellor and Yamada* [1982] turbulence closure parameterization (appendix). Their background value is chosen as 2.0×10^{-5} m^2/s.

The σ coordinate approach is known to introduce some errors in the velocity and density fields in regions of steep topographical changes [*Haney*, 1991]. As reported by *Gerdes* [1993], z-level models have similar errors for sharp topographies. In the appendix we summarize results relevant to the performance of the σ-coordinate approach and the measures used in this study to reduce the pressure gradient errors associated with the steep topography and strong stratification of the Black Sea.

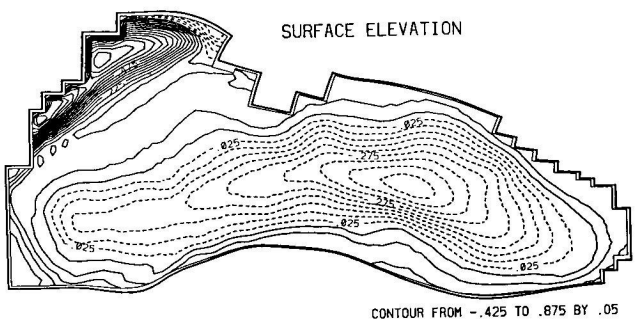

Figure 8. Surface elevation pattern (in centimeters) for the wind-driven circulation in barotropic ocean (day 600, experiment 1).

4.1. Circulation Driven by Wind Stress Alone

In this section we investigate the driving of the circulation by the wind stress excluding all other forcing mechanisms. Experiments with the baroclinic ocean are carried out first over a flat bottom and then including the topography. Using basin-averaged values of the temperature and salinity (9.0°C and 21.6 ppt), the barotropic wind-driven circulation (Figure 8) has a basin scale cyclonic cell and a small anticyclonic gyre on the shallowest part of the northwestern shelf region. The center of the cyclonic cell is situated within the eastern basin where it reaches its maximum intensity. This interior cell, in fact, will emerge as one of the robust subbasin scale features, in addition to the outer cell around the periphery, of the wind-driven baroclinic experiments described below. The surface currents are dominated by local Ekman transport and are, at most, 5 cm/s along the periphery of the anticyclone and ~2 cm/s within the cyclonic cell. The contribution from the barotropic geostrophic currents due to the sea surface height effectively vanishes at the surface. In the lower layers, where the Ekman transport is gradually weakened, the circulation pattern becomes similar to the depth-averaged circulation inferred from the surface elevation field (Figure 8). Unrealistically weak depth-averaged currents are always a result of the use of a purely barotropic model [*Malanotte-Rizzoli and Bergamasco*, 1989, 1991],

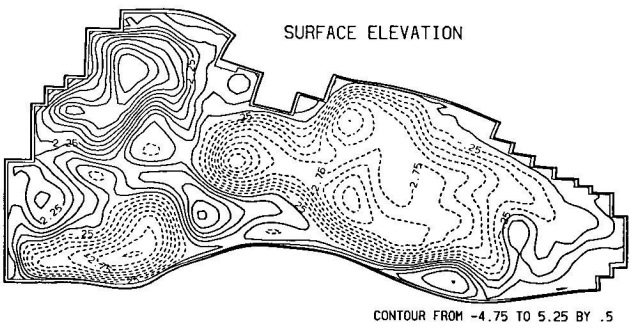

Figure 9. Surface elevation pattern (in centimeters) for the wind-driven circulation in flat bottom, baroclinic ocean (day 720, experiment 2).

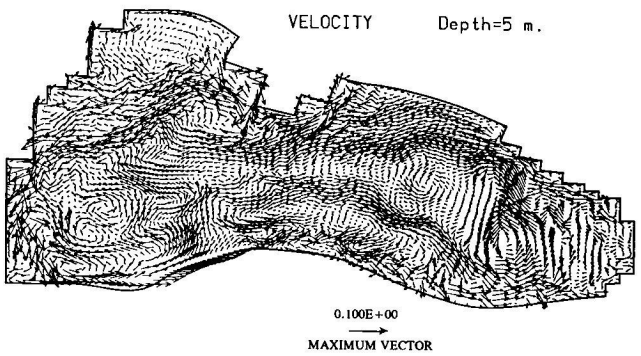

Figure 10b. The 5-m wind-driven circulation pattern with topography in baroclinic ocean (day 1080, experiment 3). Maximum current speed is set to 10 cm/s for clarity of presentation of the circulation.

apart from the noted weakness of the *Hellermann and Rosenstein* [1983] winds.

Stratification, in a mean basin depth of 1400 m, produces a fourfold increase in the strength of the circulation and enhanced structural variability. The major features of the depth-averaged circulation (Figure 9) are the basin-wide cyclonic cell and the adjacent anticyclonic northwestern region. An offshore jet protrudes in a southeasterly direction from the anticyclonic shelf gyre and breaks the interior cyclonic cell into two parts, giving rise to an isolated cyclonic gyre in the southwestern part of the basin. Consistent with the complex pattern of surface elevation, a highly meandering boundary current system is evident in the surface circulation map.

The surface circulation pattern does not change much within the upper 150 m. In the lower layer (not shown) the closed circulation cell disintegrates into two pairs of cyclonic and anticyclonic multilobed subbasin scale gyres interconnected by meandering midbasin currents. This flow structure resembles the intermediate-depth circulations deduced from the dynamic height computations [*Oguz et al.*, 1993, 1994]. An implication of this similarity is that the observed intermediate-depth circulations computed from hydrographic data would be altered significantly if the contributions from the jebar effect would be included. This would lead to stronger and possibly more organized circulation patterns, which is implied independently from the ADCP measurements [*Oguz et al.*, 1995].

Considerable modification in the flow structure takes place when topography is added to the previous experiment (Figures 10a and 10b). The currents become even stronger, reaching a maximum intensity of 20 cm/s. This strengthening of the circulation is the typical result of the jebar effect due to the interaction between topography and stratification [*Holland*, 1973]. In contrast to Figure 9, the flow now has a well-defined boundary current system confined along the steepest topographic slope of the basin. Inside the overall cyclonic circulation whose structure is controlled by the topography, there is another cell situated over the flat interior of the eastern basin. This elongated cell, as indicated before in the barotropic experiment, is a robust feature and a direct consequence of the wind forcing. Compared with Figure 9 of the flat bottom baroclinic experiment, the circulation within the northwestern shelf region is less structured, with only a smaller anticyclonic eddy occupying the northern part of the shelf. It is separated from the circulation in the deep interior through a broad current system locked to the relatively wide topographic slope region. The large meander and the associated anticyclonic eddy, which was present along the western coast in the previous experiment, is now replaced by a narrow, elongated jet extending about 100 km offshore from the shelf break, coupled to a smaller anticyclonic eddy near the coast.

Some of the features of Figures 10a and 10b are quite realistic and have their counterpart in the observational fields. Comparing with Figures 2a and 2b, important realistic features produced by the inclusion of the topography are the Batumi eddy near the southeastern corner, as well as the Sevastopol and the Crimean anticyclones located on both

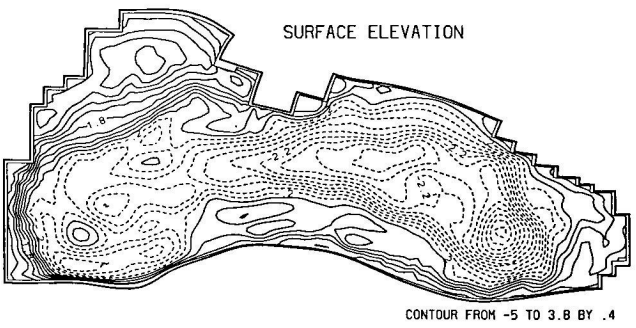

Figure 10a. Surface elevation pattern (in centimeters) for the wind-driven circulation with topography in baroclinic ocean (day 1080, experiment 3).

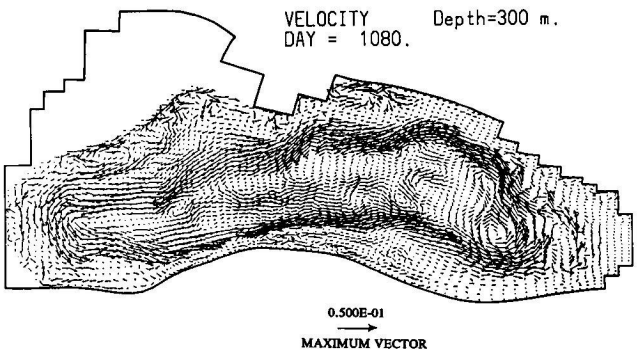

Figure 10c. Same as in Figure 10b, but at 300 m depth.

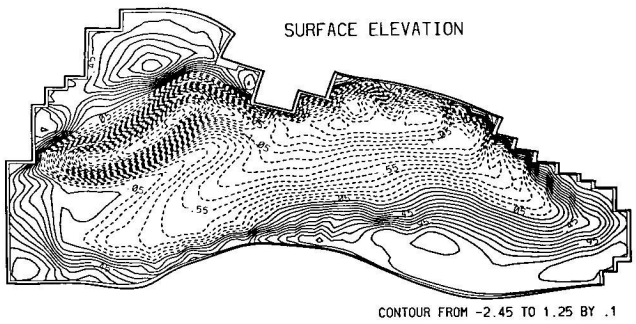

Figure 11. Surface elevation pattern generated by the annual mean E − P flux alone (day 720, experiment 4).

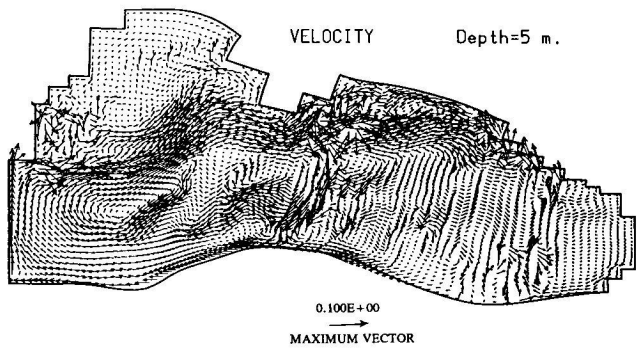

Figure 12b. The 5-m circulation pattern driven by the combination of annual mean heat flux and the E − P flux (day 1080, experiment 5). Maximum current speed is set to 10 cm/s for clarity of presentation of the circulation.

sides of the Crimean peninsula. The two filaments along the Turkish coast are also the type of features frequently seen in the satellite imagery. Needless to say, Figures 10a and 10b show one instantaneous snapshot of the temporally evolving structure of these filaments. The comparison of Figure 9 (flat bottom) and Figures 10a and 10b (actual topography) shows the crucial importance of the relief in controlling the overall circulation in a basin like the Black Sea, characterized by steep slopes all around the periphery.

The surface circulation (Figure 10b) extends uniformly within the upper layer of ~150 m. Below the pycnocline, two important modifications take place in the flow structure. As shown in the 300-m circulation pattern (Figure 10c), the basin-wide cyclonic circulation is characterized by only its inner cell. The outer cell around the periphery is now replaced with an anticyclonic recirculation zone. Along the Turkish coast the eastward flow splits into two branches to the right of the Bosphorus. In addition to the inner branch which constitutes the main interior current system, there is a second branch following closely over the margin topography. These two branches join again later near the eastern end of the basin. The interior cyclonic cell has now a meandering structure, coupled with a succession of interconnecting cyclonic eddies. The coastal recirculation zone consists of a series of distinct anticyclonic eddies, having comparable sizes with the cyclones of the basin's interior. This structure persists within the entire lower layer, with a narrowing anticyclonic zone in the deeper levels.

4.2. Circulation Driven by Surface Fluxes Alone

The circulation driven only by the net annual mean E − P flux (Figure 11) is a mirror image of the E − P distribution given in Figure 7b. It is characterized by a broad anticyclonic region near the southeastern corner, also extending farther west along the Turkish coast. A similar anticyclonic circulation is present in the northwestern shelf and the southwestern region. This latter anticyclone is of thermohaline origin, whereas the former located on the shallow shelf is due to anticyclonic relative vorticity generated by the shallowing topography to the right of the flow. The interior of the basin is governed by a cyclonic circulation cell. The strongest currents of ~10 cm/s are observed along the Caucasian and Crimean coasts over the steep topographic slope, as well as on the wide continental slope region connecting the northwestern shelf to the interior. These regions of stronger currents are associated with two elongated cyclonic eddies corresponding to the cores of two positive maxima in the E − P flux (Figure 7b); the western eddy is further modified by the regional topography. The surface salinity field is consistent with the circulation pattern of Figure 11. The southeastern part having negative E − P fluxes attains the lowest salinity values ($\lesssim$18.0 ppt), whereas the cyclonic eddies correlated with the maxima of E − P fluxes are characterized by greater salinities ($\gtrsim$18.8 ppt).

When the surface heat flux is added to the E − P flux in the buoyancy forcing, the circulation changes in response to the prescribed heat flux distribution (Figures 12a and 12b). The southern part of the sea, which is characterized by positive

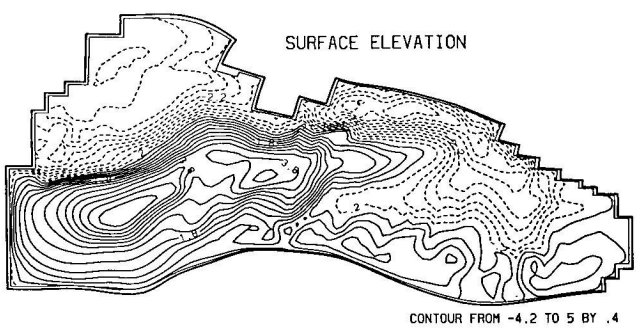

Figure 12a. Surface elevation pattern generated by the combination of annual mean heat flux and the E − P flux (day 1080, experiment 5).

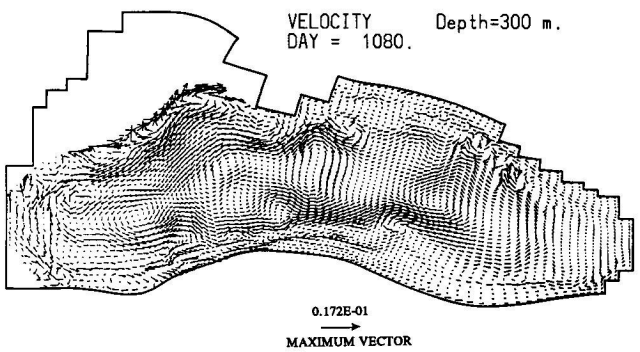

Figure 12c. Same as in Figure 12b, but at 300 m depth.

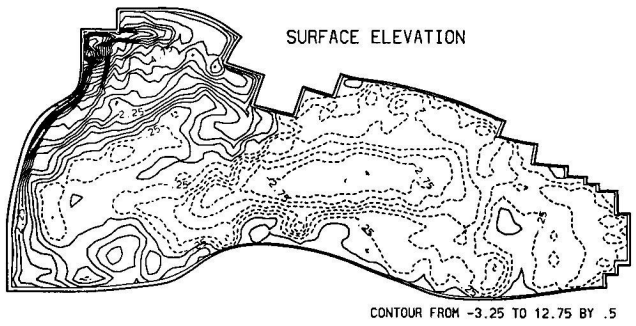

Figure 13a. Surface elevation pattern generated by the freshwater inflow from the Danube alone (day 1080, experiment 6).

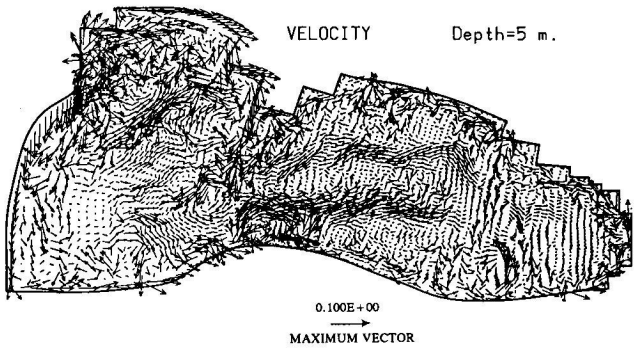

Figure 13b. The 5-m circulation pattern driven by the freshwater inflow from the Danube alone (day 1080, experiment 6). Maximum current speed is set to 10 cm/s for clarity of presentation of the circulation.

yearly mean total heat flux Q (i.e., warming), as well as smaller net positive E − P flux (i.e., weaker evaporation), is dominated by an anticyclonic circulation. An anticyclonic cell occupies almost entirely the western basin and replaces the cyclonic western cell of Figure 11. On the other hand, the northwestern shelf, subject to the strongest cooling, has a cyclonic circulation with typical currents of ~10–15 cm/s, i.e., a pattern reversed with respect to the anticyclonic shelf gyre of Figure 11. The Caucasian coast, which is also affected by strong cooling, is also characterized by a cyclonic circulation. The latter cell extends toward the interior of the eastern basin due to the additional contribution of the evaporation that favors a cyclonic circulation. On the other hand, the southern part of the eastern basin is still (weakly) anticyclonic due to the warming and precipitation excess over this region.

The considerable north-south variability of the heat flux is also reflected in the temperature distribution. The northern part of the basin has temperatures <10.0°C, reducing to ~3°C over the shallower northwestern shelf. The anticyclonic regions tend to be much warmer, having temperatures greater than ~15°C, that reach a maximum of 18.0°C within the centers of the anticyclones. A strong thermal front extends throughout the basin almost diagonally in the northwest-southeast direction.

The differences between the circulation patterns of Figures 12a and 12b and Figure 11 are quite substantial and striking. These experiments clearly indicate that the surface heat fluxes are a stronger forcing function than the surface water fluxes and hence drive the thermohaline circulation. As we shall see in experiments 7 and 8a, this thermohaline circulation dominates its wind-driven counterpart.

The circulation, however, is substantially different in the lower layer. The anticyclonic loop weakens gradually with depth within the upper 200 m and then changes sign at deeper levels. The circulation at 300 m (Figure 12c) is now cyclonic and strikingly similar to the wind-driven pattern of Figure 10c. Once again, the Rim Current forms one meandering cyclonic cell, with a series of cyclonic and anticyclonic eddies on its interior and coastal sides, respectively.

4.3. Circulation Driven by Freshwater Inflow Alone

In this section we discuss an experiment designed to investigate the contribution of lateral buoyancy flux due to river outflow on the northwestern shelf switching off both the wind and the surface thermohaline forcings simultaneously. We open the Bosphorus Strait in the southwestern corner, allowing for inflow/outflow forcing. The dramatic effect of the Danube inflow on the large-scale circulation of the Black Sea is shown in Figures 13a–13c. Although the freshwater input is only 10,000 $m^3 s^{-1}$, the buoyancy source introduces strong baroclinic pressure gradients, which then generate a strong depth-integrated flow along the coast, following isobaths (Figure 13a) under the action of the jebar effect (bottom pressure torque) [*Hendershott and Malanotte-Rizzoli*, 1976; *Shaw and Csanady*, 1983; *Vennell and Malanotte-Rizzoli*, 1990]. This process, first effective in the vicinity of the source region, spreads in time over the entire basin and then ultimately gives rise to a well-developed, strongly meandering Rim Current all around the periphery of the sea. This branch of the current system has the form of a narrow coastal jet of width comparable to the baroclinic radius of deformation of ~20 km and a typical speed of 15 cm/s at the surface. The meanderings are particularly pronounced along the southern boundary and often accompanied by the formation of a series of anticyclonic centers that are well-observed features of the surface circulation [*Oguz et al.*, 1993, 1994; *Sur et al.*, 1995]. The amplitude of the meanders along the Caucasian coast is smaller, and the Rim Current is narrower and more attached to the coastline. The interior circulation is characterized by one elongated cyclonic cell that gradually weakens westward by filament intrusions from both the southern and northern coasts of the western basin.

Locally, the Danube inflow drives a strong anticyclonic circulation over the northwestern shelf having maximum speed of ~30 cm/s. It extends to the western coast of the

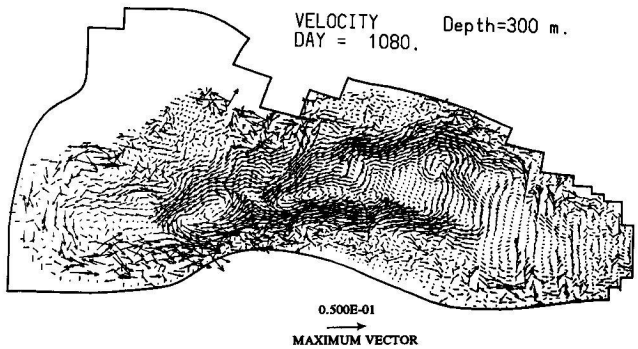

Figure 13c. Same as in Figure 13b, but at 300 m depth.

Crimean Peninsula and contributes to the Sevastopol anticyclonic eddy. The anticyclonic circulation cell is closed by a southwestward current flowing along the topographic slope separating the deeper interior from the shelf. This slope current is essentially of shelf origin and contributes only slightly to the basin's jetlike peripheral circulation system.

The features and processes taking place on the shelf constitute a typical example of buoyant outflows, whose dynamics were studied theoretically by *Gill* [1976], in laboratory experiments by *Whitehead and Miller* [1979] and *Whitehead* [1985], and in numerical model studies by *Chao and Boicourt* [1986] and *Wang* [1987]. The latter calculations explained the formation mechanism as a result of potential vorticity conservation.

The circulation system induced by the lateral buoyancy source is accompanied by considerable temperature and salinity variability throughout the basin (Figures 14a and 14b). A major thermohaline feature of the system is the sharp frontal structure established along the coast, as well as along the topographic slope between the northwestern shelf and the interior of the western basin. The 5-m temperature distribution (Figure 14a) clearly displays this frontal zone between relatively colder, upwelled interior waters and the warmer coastal waters, with a temperature contrast of nearly 3°C. On the other hand, the shelf interior has a more homogeneous vertical structure (Figure 15, top), characterized by relatively uniform temperatures of ~12°C, except in the close vicinity of the source region. This is due to the small temperature difference between the source itself and ambient waters. For the same reason, the temperature contrast between the shelf and deep basin is also relatively weak. Contrary to the stronger shelf break salinity front (Figure 15, bottom), the cross-frontal temperature gradient is only ~1°C.

The surface horizontal salinity distribution (Figure 14b) evidences more clearly than temperature the overwhelming influence of the river discharge in the northwestern shelf, as well as its extensions along the Bulgarian and Turkish coasts. The most dramatic variations take place within the core of the shelf anticyclone characterized by a strong inner shelf salinity front along its rim (Figure 15, bottom). The bulge has a thickness of 30 m, with more than 8 ppt salinity difference over a distance of ~50 km (Figure 15, bottom). The outer shelf has comparatively weaker salinity variations, and a second front is evident at the shelf break. The combined frontal structure extends all along the west coast

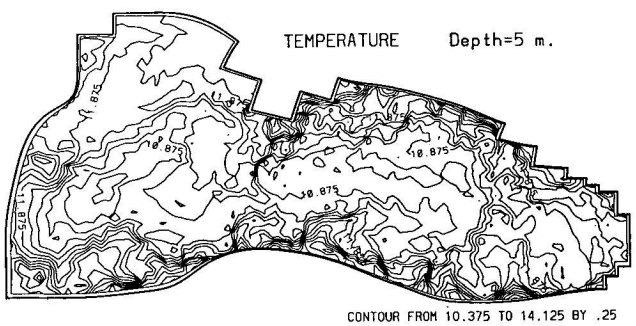

Figure 14a. The 5-m temperature distribution for the circulation driven by the freshwater inflow from the Danube alone (day 1080, experiment 6).

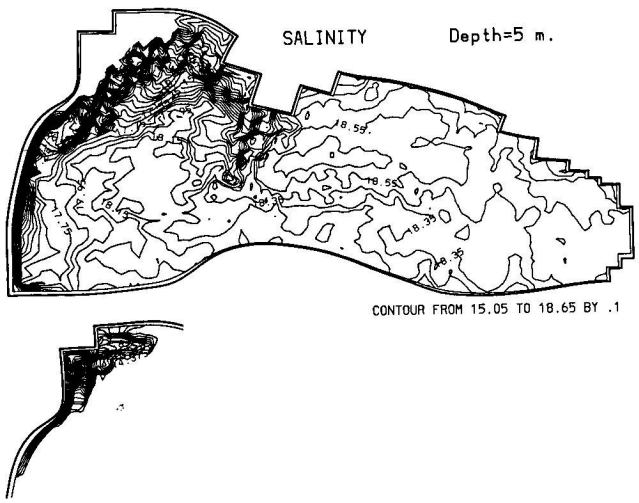

Figure 14b. The 5-m salinity distribution for the circulation driven by the freshwater inflow from the Danube alone (day 1080, experiment 6) showing (top) interior distribution and (bottom) northwest corner with the distribution on the shelf.

up to the Bosphorus Strait region, where it is terminated abruptly by the inflow/outflow conditions specified at the Bosphorus opening. Farther in the interior and eastward, the salinity signature of the inflow gradually weakens, and thus the salinity contrast between the Rim Current and the interior water mass becomes less pronounced (<0.3 ppt).

The two-way exchange taking place within the Bosphorus Strait modifies locally the freshwater-driven upper layer circulation. As shown in Figures 13a and 13b, the surface flow bifurcates immediately outside the Bosphorus. The main flow proceeds in an eastward direction but also partially leaves the basin from the Bosphorus opening. An implication of this flow divergence is an upward vertical motion near the opening, with subsequent generation of a cyclonic eddy (see Figure 14a) through the cooling of surface waters produced by the upwelling of colder subsurface waters. Beneath the cyclonic eddy the Mediterranean water flows into the basin near the bottom and spreads into the southwestern basin.

The lower layer circulation developed in response to the combination of the Danube inflow and Bosphorus inflow/outflow is again overall very similar to those of the wind and thermally driven experiments shown earlier in Figures 10c and 12c, respectively. As shown in the 300-m pattern (Figure 13c), it comprises the elongated cyclonic cell of the Rim Current, surrounded by an anticyclonic region formed by a series of anticyclonic eddies along the entire coast. The interior circulation, however, now has a slightly different meandering pattern characterized by smaller-sized eddies and slightly shorter waves.

Even though the model handles quite successfully the two-way interactions at the Bosphorus opening, it has limitations in resolving complex mixing processes taking place in a relatively short distance of ~40 km across the shelf [*Latif et al.*, 1991; *Oguz and Rozman*, 1991; *Ozsoy et al.*, 1994]. Unless this general circulation model is coupled with a fine resolution regional model of the Bosphorus exit region incorporating the relevant dynamics of complex mixing processes, the evolutionary characteristics of the Mediterra-

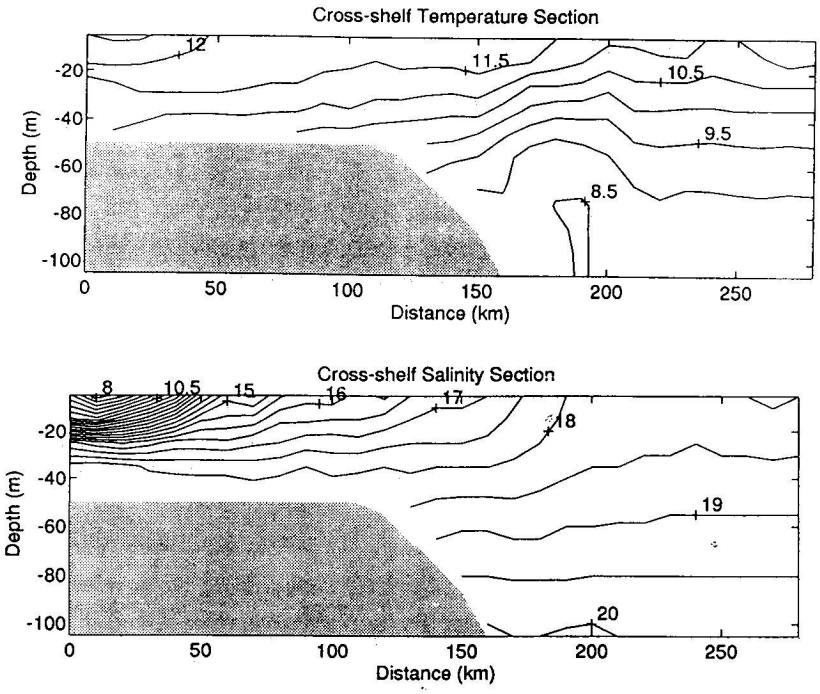

Figure 15. (top) Temperature and (bottom) salinity transects across the middle of northwestern shelf for the circulation driven by the freshwater inflow from the Danube alone (day 1080, experiment 6).

nean underflow in the Black Sea will remain unexplored. In the present model the Bosphorus opening serves basically to satisfy continuity requirements. In spite of this limitation, this experiment clearly demonstrates that the buoyancy source forcing on the shelf and the inflow/outflow forcing at the Bosphorus are responsible for the development of the intense jetlike meandering Rim Current and of the sharp temperature and salinity fronts on the inner shelf and the shelf break.

4.4. Multiple Forcing Experiments

4.4.1. Central experiment. The circulation and TS surface distributions of the central experiment (Figures 16a, 16b, 17a, and 17b) clearly reflect the superposition of the separate effects generated independently by the three forcing mechanisms discussed in detail in the previous sections. The weakest signal in Figures 16a–17b is the wind-driven component, as demonstrated by the marked differences between Figures 16a and 16b and Figures 10a and 10b. The most pronounced signal, on the other hand, comes from the surface heat flux, as evident from the cooling and associated cyclonic circulation in the northwestern shelf, the warming and associated anticyclonic circulation in the southern part of the western basin.

4.4.1.1. Upper layer circulation: The circulation on the northwestern shelf region is the result of the opposing effects of surface thermal forcing and the lateral buoyancy input. The cooling of the shelf waters tends to generate a cyclonic circulation (Figure 12a) and reverses the anticyclonic cell due to the Danube forcing (Figure 13a). The bulge that develops near the Danube outflow has a smaller size, and the related frontal structure is weaker. The effect of the fresh water is mainly confined to the inner shelf region. The shelf break front developed in the freshwater-driven circulation (Figures 13a and 13b) now shifts into the shelf interior and strengthens the inner shelf front. The outer edge of this

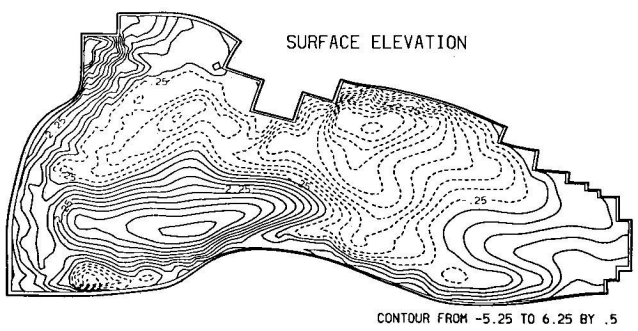

Figure 16a. Surface elevation pattern generated by the combination of all the three forcings (day 1050, experiment 7).

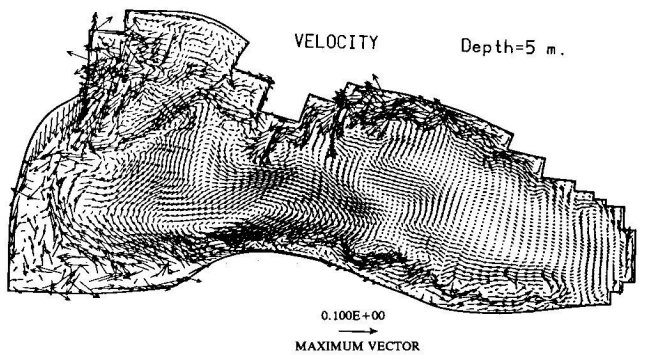

Figure 16b. The 5-m circulation pattern driven by the combination of all the three forcings (day 1050, experiment 7). Maximum current speed is set to 10 cm/s for clarity of presentation of the circulation.

strong front is marked by the 18 ppt isoline in the salinity distribution of Figure 17b. Even though restricted to the coastal region, the currents generated from the freshwater inflow still form an anticyclonic loop and penetrate to the tip of the Crimean peninsula. Together with the Rim Current, they contribute to the formation of the Sevastopol eddy.

The lack of the shelf break front allows interaction of outer shelf waters with the interior of the basin. The large-scale cyclonic circulation now extends into the outer shelf where it forms a broad midbasin current, after combining with the branch of the anticyclonic cell. In the temperature distribution of Figure 17a the protrusion of the cyclonic circulation into the shelf is reflected by the sharp temperature contrasts of >2°C, both on the inner shelf and the anticyclonic gyre sides. This experiment indicates that a possible mechanism for the destruction of the shelf break front is a prolonged cooling of the region, with north to south variability in the heat flux. As demonstrated in section 4.4.3, a horizontally uniform seasonal cooling, even though stronger during the winter period, does not lead to destruction of the shelf break front with consequently no shelf–deep basin exchange.

The presence of the anticyclonic cell also alters, to some extent, the features of the wind-driven and the buoyancy-driven circulations along the west coast of the basin. The boundary current due to the Danube inflow and the two separate currents flowing southwestward over the topographic slope (the first associated with the inner shelf front, the second a part of the cyclonic circulation cell) converge with the oppositely flowing currents of the anticyclonic cell near Cape Kaliakra. There the current southward flowing over the topographic slope along the Bulgarian coast is considerably weakened when compared with Figures 13a and 13b and is replaced by an elongated cyclonic eddy. Near the southwestern corner a small anticyclonic eddy frequently observed at this location [cf. *Oguz et al.*, 1993] is developed.

The eastern half of the Turkish coast has a meandering Rim Current and three coastal anticyclonic eddies, followed by the subbasin scale Batumi anticyclone. The present structure of the Batumi anticyclone is due to the combined effects of the wind stress and surface thermohaline fluxes. This implies that the eddy has a quasi-permanent character, although its size and intensity undergo seasonal variations depending on the relative contributions of the two individual forcings.

The annual mean cooling enhances the cyclonic tendency induced by the annual mean wind stress and generates a

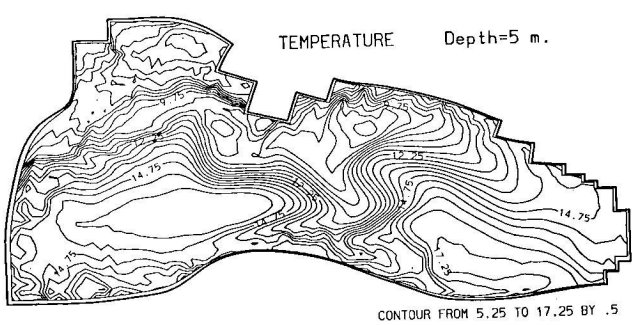

Figure 17a. The 5-m temperature distribution for the circulation driven by the combination of all the three forcings (day 1050, experiment 7).

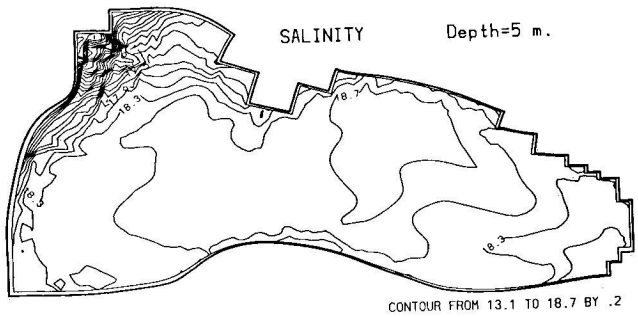

Figure 17b. The 5-m salinity distribution for the circulation driven by the combination of all the three forcings (day 1050, experiment 7).

cyclonic gyre in the eastern basin which has a much larger meridional size than in the purely wind-driven pattern (Figures 10a and 10b). The Rim Current is now attached to the coast with a distinct meandering structure over the topographic slope along the Caucasian coast. The jetlike behavior of the current continues along the Crimean coast, where it tends to split into several branches. The branch that joins the interior circulation is different in each of the individual experiments. But there is always a branch locked to the local continental slope, flowing southwestward adjacent to the northwestern shelf.

The cyclonic cell of the central basin has a salinity >18.5 ppt. The anticyclonically dominated regions are identified on its sides with values of 18.2–18.4 ppt. The temperature front between the two cells with ~5°C change over a distance of ~50 km forms one of the strongest thermohaline features of the system. The similar frontal structure with ~1.5°C temperature contrast, observed in the September 1990 hydrographic survey [see *Oguz et al.*, 1993, Figure 4], might be associated with the signature of the heat flux component of the circulation.

The most unrealistic feature of the central experiment circulation is the formation of the anticyclonic gyre in the western basin and the subsequent breaking of the Rim Current. An anticyclone formation of this size has never been observed either in the climatological maps or in our few medium-resolution (~36 km) hydrographic surveys. This might be due to the compensation of the heat flux forcing by a stronger wind-driven component on the yearly average. Alternatively, the annual mean of the circulation generated by the seasonally varying heat flux might be different from that induced by the annual mean of the heat flux. These two possibilities are explored by two numerical experiments with stronger wind stress forcing and a seasonally varying heat flux.

4.4.1.2. Lower layer circulation: As in previous sections, the structure of the lower layer circulation remains the same, irrespective of the type of the forcing. The three forcing mechanisms examined here tend to affect the upper layer of, at most, ~200 m. The strong pycnocline then isolates their effects on deeper levels. We show now circulation patterns to display how the structure of the surface circulation of the central experiment is modified with depth. A discussion on the sensitivity of the relatively weak deep circulation to the pressure gradient approximations across the topographic slope is given in the appendix.

The main features of the circulation at 100 and 300 m

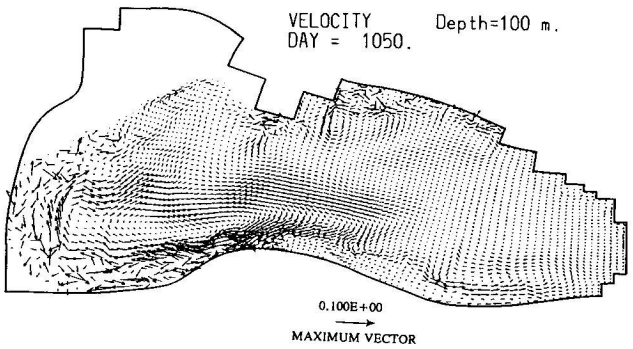

Figure 18a. The 100-m circulation pattern driven by the combination of all the three forcings (day 1050, experiment 7). Maximum current speed is set to 10 cm/s for clarity of presentation of the circulation.

(Figures 18a and 18b) are similar to those of the surface pattern (Figure 16b). However, some features undergo some changes with depth. The most noticeable modification is the gradual shrinking of the western anticyclonic cell, as its northern branch shifts farther south toward the Turkish coast. As it thins, it also extends farther eastward, and the basin circulation is now composed of two zonally elongated, oppositely flowing cells. The meanders of the coastal current also become wider. This is noticeable, in particular, for the westward flow along the northern coast whose main axis shifts slightly to the south, giving rise to a local anticyclonic eddy off the Azov Sea.

At a depth of 300 m the eastward flowing midbasin current system shifts even farther south (Figure 18b). Consequently, the southern anticyclonic cell reduces to a narrow anticyclonic coastal zone along the Turkish coast. A similar anticyclonic recirculation zone also begins to develop along the northern coast of the basin. The only major signature left from the surface subbasin scale anticyclonic gyre is the detached anticyclonic eddy that disappears at deeper levels. The implication is that the circulation below ~300 m is basically barotropic, driven by the surface elevation (Figures 10a, 12a, 13a, and 16a) whose patterns are similar for all the forcings investigated here. Hence the baroclinic component of the circulation generated in response to the deformation of the pycnocline is only limited to a transitional layer immediately below the pycnocline. In the numerical experiments described here this transition zone is identified between the depths of 150 and 300 m. It might, however, extend slightly deeper if the observed spatial variability of the density at depths between 200 and 400 m were incorporated initially in the model.

4.4.2. Strong wind forcing case. One rather unrealistic result of these simulations is the weak circulation driven by the *Hellermann and Rosenstein* [1983] climatology, as compared to that reproduced by the prognostic calculations that use different wind stress fields [e.g., *Stanev et al.*, 1995; Meacham, submitted manuscript, 1994]. We therefore investigate the response of the general circulation pattern under stronger wind forcing, assuming that the surface thermohaline fluxes used reflect the realistic climatological yearly mean conditions. To understand which is the mechanism responsible for the unrealistic anticyclone, we first cut off the Danube discharge and inflow/outflow at the Bosphorus. In experiment 8a, carried out with a combination of wind stress and surface fluxes in a closed basin, the circulation is similar to that obtained in the central experiment including the anticyclonic gyre in the southwestern basin. Thus the freshwater discharge of the Danube does not induce this unrealistic feature of the circulation, as evident also from Figures 13a and 13b, and is excluded from the successive experiments 8b and 8c. In experiment 8b the same annual surface thermohaline fluxes are used, as well as the same spatial distribution of the wind stress, but with an intensity 5 times stronger. This increases the maximum strength of the wind stress to ~1 dyn/cm^2, with typical magnitudes of ~0.5 dyn/cm^2. Winds with such intensity are rather common during winter [*Staneva*, 1993], even though they may be too strong on the climatological basis.

With this strong wind climatology the maximum currents reach ~60 cm/s, with typical values of ~25 cm/s. The stronger cyclonic tendency induced by the wind in the basin interior overcomes the anticyclonic circulation generated by the heat flux in the central part of the western basin (Figure 19). The cyclonic circulation of the northwestern shelf (NWS) is also reversed to anticyclonic. There is now a continuity of the Rim Current all around the basin. The circulation pattern is similar to that obtained in the purely wind-driven experiment (Figure 10a). Common features are the meandering Rim Current, an anticyclonic eddy at the southeastern corner, a cyclonic gyre at the southwestern end, and an elongated cyclonic cell occupying the rest of the basin's interior. The Bosphorus, Kizilirmak, Crimean, and Sevastopol anticyclonic coastal eddies are also present in the

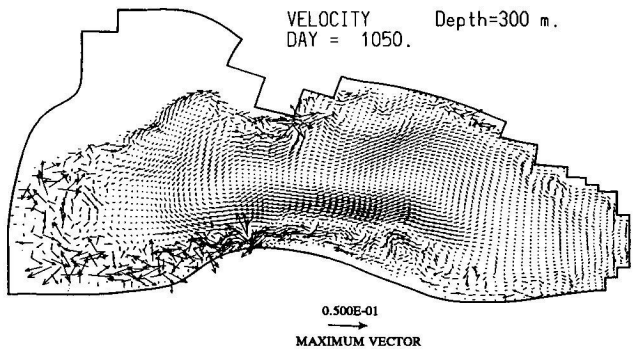

Figure 18b. The 300-m circulation pattern driven by the combination of all the three forcings (day 1050, experiment 7). Maximum current speed is set to 5 cm/s for clarity of presentation of the circulation.

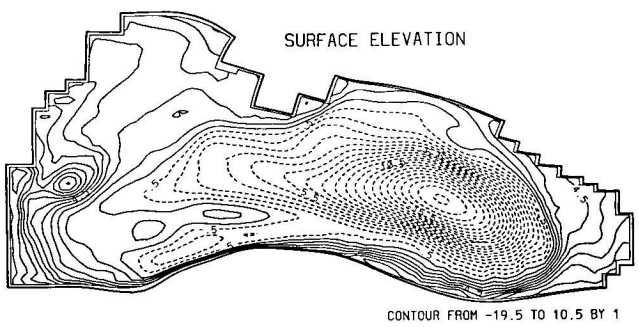

Figure 19. Surface elevation pattern generated by the combination of the strong wind stress and surface flux forcings (day 1080, experiment 8b).

circulation pattern, as well as the small, elongated anticyclonic eddy centered at 33°E longitude offshore of the Turkish coast. The latter one is an eddy pinched off from the locally growing meander of the Rim Current. The Kaliakra eddy, which was small and confined to the Bulgarian coast, emerges here as a well-developed structure located farther from the coast.

4.4.3. Seasonally varying heat flux forcing case. In experiment 8c, the second possibility causing unrealistic anticyclone is studied. Even though the north-to-south variability of the yearly climatological heat flux pattern may be similar to the one shown in Figure 7a, this spatial variability may be dynamically less important than the time variability. We thus keep the weak *Hellermann and Rosenstein* [1983] winds but apply a horizontally uniform heat flux with a seasonal cycle, representing approximately the basin-averaged seasonal heat flux variations [*Staneva*, 1993].

With the yearly cycle of heat flux prescribed the depth-averaged circulation for the end of February and end of August (Figures 20a and 20b) consists of a well-defined meandering Rim Current along the boundary of the basin, as well as an elongated cyclonic cell centered in the eastern basin, as in experiment 8b. This pattern is much more realistic and qualitatively similar to the patterns obtained from climatological data, as well as recent hydrographies (Figures 1, 2a, and 2b).

The NWS circulation is now anticyclonic throughout the year, even in the period of maximum cooling rate during the winter months. As expected, the anticyclonic tendency of the shelf is stronger during the summer months, corresponding to the increase in heat flux. This anticyclonic pattern would be reinforced by the Danube freshwater inflow (Figure 13a).

5. Conclusions

In the present work, numerical experiments were carried out to identify the relative contributions of the three primary forcing mechanisms in driving the large and mesoscale components of the Black Sea circulation, depending on their intensity and spatial distributions. Using standard climatological data sets (wind stress of *Hellermann and Rosenstein* [1983] and surface fluxes of *Altman et al.* [1987]), the three dominant driving mechanisms (the wind stress, the surface thermohaline fluxes, and lateral buoyancy fluxes from the Danube and the Bosphorus) were studied first in isolation and then in their various combinations.

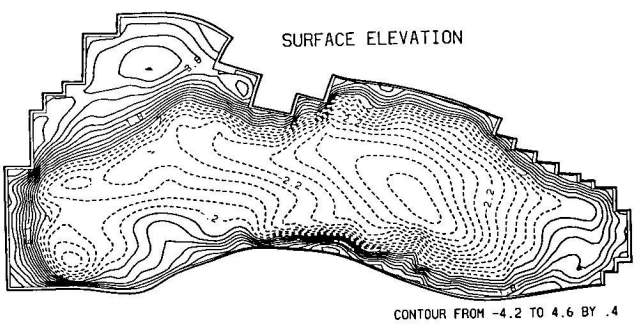

Figure 20a. Surface elevation pattern generated by the combination of the wind stress and temporally varying but horizontally uniform heat flux forcings for the end of February (day 1250, experiment 8c).

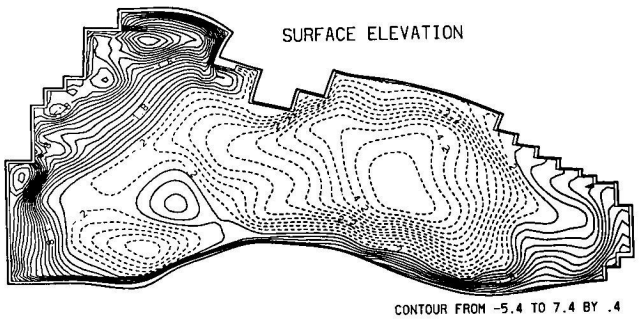

Figure 20b. Surface elevation pattern generated by the combination of the wind stress and temporally varying but horizontally uniform heat flux forcings for the end of August (day 1430, experiment 8c).

The comparison of experiments with a flat bottom and with realistic relief shows the crucial importance of topography in controlling the overall circulation. In the upper layer of ~150 m the topography controls the well-defined narrow band of the boundary current system (the Rim Current) confined over the steepest topographic slope.

Of the three forcing mechanisms studied the weakest signal in the yearly mean circulation comes from the wind-driven component due to the well-known weakness of the *Hellermann and Rosenstein* [1983] winds for the Black Sea. Winds contribute more strongly to the mean circulation when they are scaled to approximate more closely the observations. The lateral buoyancy forcings from the Danube and the Bosphorus develop an intense, meandering Rim Current with temperature and salinity fronts along the periphery, as well as the associated mesoscale eddy field. The Danube inflow drives a strong anticyclonic circulation on the northwestern shelf between two well-pronounced salinity fronts. The outer front separates the shelf from the basin's interior across the shelf break, whereas the inner front decouples the shelf from the local influence of the freshwater discharge near the source region.

The annual mean surface heat flux constitutes a stronger forcing than both the surface water fluxes and the modeled wind stress and is the major agent driving the thermohaline circulation. The north-to-south variability of the heat flux results in a circulation pattern formed by a cyclonic cell in the northern half and an unrealistic anticyclonic gyre in the southwestern part of the basin. Stronger wind forcing, however, eliminates the anticyclonic gyre, as the wind stress tends to enhance a cyclonic circulation. The anticyclonic gyre is also eliminated when a horizontally uniform but seasonally varying surface heat flux is used together with annual climatological wind stress. This result strongly suggests that the seasonal cycle of the wind stress is much less crucial than the heat flux seasonal cycle in producing a realistic basin circulation.

The model circulation has a basic two-layer structure, with vertical homogeneity within each layer. In the upper layer many of the known features of the circulation are realistically reproduced, especially in the experiment with the heat flux seasonal cycle. The Rim Current and the interior cyclonic cell are the building blocks of the basin

scale circulation. The anticyclonic gyres on the northwestern shelf and the southeastern corner, as well as the cyclonic gyres within the interior, are the main subbasin scale features. The series of anticyclonic eddies confined between the coast and the meandering Rim Current constitutes part of the mesoscale variability. Other mesoscale features originate from the evolution of propagating meanders that give rise to intense offshore filaments and detached eddies.

The circulation in the lower layer (below 300 m) is separated from that of the upper layer by a transition zone and is independent of the type of forcing specified at the surface and/or lateral boundaries. The lower layer circulation intensifies, but the structure remains unchanged in the experiment with strong wind stress forcing. Obviously, the duration of the numerical experiments, even though sufficient to spin-up the wind-driven component, is not long enough to allow for full adjustment of the deep thermohaline circulation. The abyssal layers circulation obtained cannot, however, be the memory of the initial conditions as we start from horizontal homogeneity of the temperature and salinity fields. Therefore the uniqueness of the deep circulation pattern is a response to the barotropic pressure gradient that develops in models allowing for a free surface, irrespective of the type of surface forcing. The deep pattern may not correspond to the actual Black Sea thermohaline circulation, even though the observational evidence of vertical homogeneity below ~300 m suggests that this thermohaline component may be very weak. The deep pattern consists of an elongated meandering cyclonic cell over the flat interior and an anticyclonic recirculation zone over the topographic slope between the inner cyclonic cell and the coast. The transition zone reflects essentially the motion induced by the horizontal variability of the pycnocline and varies depending on the intensity and horizontal structure of the surface fluxes, as well as the form of the initial stratification.

Appendix: Model Formulation

A1. Governing Equations

The sigma transformation is defined by $\sigma = (z - \zeta)/(h + \zeta)$. The free surface $z = \zeta$ is then represented by $\sigma = 0$ surface, whereas $\sigma = -1$ corresponds to the seafloor at $z = -h(x, y)$. The orthogonal horizontal curvilinear coordinates $\xi(x, y)$ and $\eta(x, y)$ are related to the Cartesian coordinates by $(ds)_\xi = md\xi$, and $(ds)_\eta = nd\eta$, where $m(\xi, \eta)$ and $n(\xi, \eta)$ represent the metric coefficients of the transformation. Defining new variables $H = h + \zeta$, $(\tilde{u}, \tilde{v}, \tilde{C}) = Hmn(u, v, C)$, the set of equations governing the motion is expressed in their flux form as

$$\frac{D\tilde{u}}{Dt} - (f - \Gamma)\tilde{v} = -\frac{Hn}{\rho_0}\frac{\partial p}{\partial \xi} + \frac{1}{H^2}\frac{\partial}{\partial \sigma}\left(K_m \frac{\partial \tilde{u}}{\partial \sigma}\right) + F_u \tag{A1a}$$

$$\frac{D\tilde{v}}{Dt} + (f - \Gamma)\tilde{u} = -\frac{Hm}{\rho_0}\frac{\partial p}{\partial \eta} + \frac{1}{H^2}\frac{\partial}{\partial \sigma}\left(K_m \frac{\partial \tilde{v}}{\partial \sigma}\right) + F_v \tag{A1b}$$

$$\frac{D\tilde{C}}{Dt} = \frac{1}{H^2}\frac{\partial}{\partial \sigma}\left(K_h \frac{\partial \tilde{C}}{\partial \sigma}\right) + F_c \tag{A1c}$$

$$\omega = \int_\sigma^0 \left\{\frac{\partial \zeta}{\partial t} + \frac{1}{mn}\left[\frac{\partial}{\partial \xi}\left(\frac{\tilde{u}}{m}\right) + \frac{\partial}{\partial \eta}\left(\frac{\tilde{v}}{n}\right)\right]\right\} d\sigma \tag{A1d}$$

where

$$\frac{D\tilde{\Psi}}{Dt} = \frac{\partial \tilde{\Psi}}{\partial t} + \frac{\partial}{\partial \xi}\left(\frac{u\tilde{\Psi}}{m}\right) + \frac{\partial}{\partial \eta}\left(\frac{v\tilde{\Psi}}{n}\right) + \frac{1}{H}\frac{\partial}{\partial \sigma}(\omega\tilde{\Psi}) \tag{A2a}$$

$$\Gamma = \frac{1}{mn}\left[u\frac{\partial m}{\partial \eta} - v\frac{\partial n}{\partial \xi}\right] \tag{A2b}$$

Γ is the curvature term arising from application of the coordinate transformation to the advective terms; Ψ denotes u, v or C; and u, v, ω are the velocity components in the ξ, η, σ directions, respectively. C denotes either the temperature or the salinity, ρ_0 is the reference density, $f = 2\Omega \sin\theta$ is the Coriolis parameter, with Ω denoting the Earth's angular speed of rotation and θ the latitude; K_m and K_h are the vertical eddy viscosity and diffusion coefficient, respectively. The horizontal diffusion terms, F_u, F_v, and F_c, are approximated in the Laplacian form as

$$F_\phi = mn\left[\frac{\partial}{\partial \xi}\left(\frac{n}{m}A_\phi H\frac{\partial \phi}{\partial \xi}\right) + \frac{\partial}{\partial \eta}\left(\frac{m}{n}A_\phi H\frac{\partial \phi}{\partial \eta}\right)\right] \tag{A3}$$

where A_ϕ represents the horizontal mixing coefficients for momentum and tracer.

The density is expressed as a function of the potential temperature, salinity, and pressure, $\rho = \rho(T, S, p)$, using a computationally simpler form of the UNESCO formula of the nonlinear equation of state devised by *Mellor* [1991].

In (A1a) and (A1b) the horizontal pressure gradient terms are given as

$$\frac{1}{\rho_0}\nabla p = g\nabla\zeta + \frac{gH}{\rho_0}\int_\sigma^0 \nabla(\rho - \langle\rho\rangle)\, d\sigma - \frac{g}{\rho_0}\nabla H\int_\sigma^0 \sigma\frac{\partial(\rho - \langle\rho\rangle)}{\partial \sigma}\, d\sigma \tag{A4}$$

where ∇ represents the horizontal gradient operator in the curvilinear orthogonal coordinate system, g is the gravitational acceleration, ρ is the density, and $\langle\rho\rangle = \langle\rho(z)\rangle$ is the horizontally averaged initial density field given at z levels. The barotropic component of the pressure gradient term is evaluated from the vertically integrated form of (A1a), (A1b), and (A1d).

A2. Turbulence Closure Parameterization

The vertical viscosity and diffusion coefficients K_m and K_h are parameterized using the *Mellor and Yamada* [1982] order 2.5 turbulence closure model wherein

$$(K_m, K_h) = lq(S_m, S_h) \tag{A5}$$

where l is the turbulence length scale; $\frac{1}{2}q^2$ is the turbulent kinetic energy; and S_m, S_h are stability factors. The turbulent closure is achieved by a simultaneous solution of the transport equations for the turbulent kinetic energy $\frac{1}{2}q^2$ and the turbulent macroscale $q^2 l$ expressed in the form

$$\frac{D\tilde{B}}{Dt} = mnH[\Phi] + \frac{1}{H}\frac{\partial}{\partial \sigma}\left(K_q \frac{\partial \tilde{B}}{\partial \sigma}\right) + F_B \tag{A6}$$

where $\tilde{B} = HmnB$. The $[\Phi]$ takes the either form of $[\Phi] = [P_s + P_b - \varepsilon]$ or $[\Phi] = lE_1[P_s + P_b - \varepsilon\tilde{W}]$ for the

turbulent kinetic energy and macroscale equations, respectively. The shear production P_s, the buoyancy production P_b, and the dissipation ε rates of the turbulent kinetic energy are defined by

$$P_s = K_m/H^2[(\partial u/\partial\sigma)^2 + (\partial v/\partial\sigma)^2], \quad \text{(A7a)}$$

$$P_b = \frac{g}{H\rho_0} K_h \frac{\partial\rho}{\partial\sigma}, \quad \text{(A7b)}$$

$$\varepsilon = \frac{q^3}{b_1 l} \quad \text{(A7c)}$$

and the wall proximity function is $\tilde{W} = 1 + E_2(l/L\kappa)^2$ with $(L)^{-1} = (\zeta - z)^{-1} + (h + z)^{-1}$. The κ (the von Karman constant) and b_1, E_1, and E_2 are empirical constants having values of 0.4, 16.6, 1.8, and 1.33, respectively.

The stability factors are expressed algebraically as a function of the stability parameter $G_H = -(l^2/q^2)(g/\rho_0)(\partial\rho/\partial z)$ by

$$S_H = c_1/(1 - c_2 G_H) \quad \text{(A8a)}$$

$$S_M = (c_3 + c_4 G_H S_H)/(1 - c_5 G_H) \quad \text{(A8b)}$$

where c_1–c_5 are constants. As shown by *Mellor and Yamada* [1982], the stability functions $S_M(G_H)$ and $S_H(G_H)$ limit to infinity as G_H approaches the value 0.0288.

A3. Boundary Conditions

At the sea surface, $\sigma = 0$:

$$\frac{\rho_0 K_m}{H}\left(\frac{\partial u}{\partial\sigma}, \frac{\partial v}{\partial\sigma}\right) = (\tau_{s\xi}, \tau_{s\eta}) \quad \text{(A9a)}$$

$$\frac{K_h}{H}\left(\frac{\partial T}{\partial\sigma}, \frac{\partial S}{\partial\sigma}\right) = \left[\frac{Q_H}{\rho_0 c_p}, S(\mathrm{E} - \mathrm{P})\right] i \quad \text{(A9b)}$$

$$\omega = 0, \qquad q^2 l = 0, \qquad q^2 = b_1^{2/3} u_{\tau s}^2 \quad \text{(A9c)}$$

where $\tau_{s\xi}$, $\tau_{s\eta}$ are the wind stress components, Q_H is the net surface heat flux, and E − P represents the evaporation minus precipitation rate.

At the bottom the boundary conditions are similar to those at the surface, except $\partial T/\partial\sigma = \partial S/\partial\sigma = 0$, and the bottom stress components, $(\tau_{b\xi}, \tau_{b\eta}) = \rho_0 C_D |\mathbf{V}_b|(u_b, v_b)$, replace the wind stress components. The drag coefficient C_D takes the larger of the two values given by $C_D = 0.0025$ or $C_D = \kappa^2[\ln(h + z_b)/z_0]^{-2}$, depending on the resolution of the bottom boundary layer. The z_b is the depth of the grid point nearest the bottom, and $\mathbf{V}_b$ is the velocity vector at this point. The z_0 defines the bottom roughness parameter taken to be 1 cm in the present work. The $u_{\tau s}$ and $u_{\tau b}$ are the friction velocities $[u_\tau = (\tau_\xi^2 + \tau_\eta^2)^{1/2}]$ associated with the surface wind and bottom frictional stresses, respectively.

A4. Numerical Procedure

The method of solution of the model equations is described in detail by *Mellor* [1991]. The finite difference discretization of the equations is done on the Arakawa-C grid. Leapfrog time stepping is employed for both the barotropic and baroclinic modes. The barotropic mode time step is 15 s. The baroclinic mode has a much longer time step of 15 min. The solutions of both modes are filtered by Asselin time filtering at the end of each time step to avoid time splitting of the solutions.

The usual free-slip and no-flux conditions are applied at lateral boundaries. When there is freshwater input into the basin, the depth-averaged normal velocity associated with the freshwater inflow is prescribed as the external open boundary condition, whereas the internal normal velocities are computed from the Sommerfeld radiation condition. In the Bosphorus Strait both internal and external mode velocities obey the radiation condition. During the outflow conditions the temperature and salinity are calculated from their upstream values. During the inflow conditions they are relaxed to their observed climatologies using a relaxation timescale of 2 days. This approach was found useful in avoiding the generation of transient sharp frontal features if the flow reverses its direction for short periods of time.

A5. Curvilinear Grid

The curvilinear horizontal grid is generated using the grid generation package provided by the semispectral primitive equation model [*Haidvogel et al.*, 1991]. The sea is projected onto a horizontal grid domain using the Lambert Conformal Conic projection of the National Center for Atmospheric Research (NCAR) Graphics EZMAP utility [*NCAR*, 1987]. The grid consists of 98 and 50 grid points in the zonal and meridional directions, respectively.

A6. Model's Sensitivity to σ Coordinates Over Steep Topography

Beckmann and Haidvogel [1993] discussed the performance of the σ coordinate approach for flow around a tall, isolated seamount and errors arising from the pressure gradient formulation in the steep topography/strong stratification limit. In a parallel study, *McCalpin* [1994] introduced a fourth-order accurate pressure gradient formulation which apparently led to a tenfold reduction in errors over a wide range of parameter space. *Mellor et al.*'s [1994] North Atlantic experiments with POM-indicated minor differences in the resulting circulation fields when compared with calculations where horizontal pressure gradients are computed on z-level coordinates. The error was advectively eliminated after a few years time integration, when an area-averaged density gradient was subtracted from the density field before evaluation of the density gradient on the σ coordinate grid (see (A4)). This numerical manipulation has also been used by *Haidvogel et al.* [1991].

On the basis of experience gained by previous studies, we have undertaken several measures to reduce the pressure gradient errors associated with steep topography and strong stratification. The topography is smoothed so that the slope factor $(\Delta H/H)$ is kept below a certain limit (~0.02). Since the error is proportional to both $(\Delta\sigma)^2$ and $(\Delta H/H)^2$ but is much more sensitive to $(\Delta H/H)$ [*Mellor et al.*, 1994], it may be reduced with increased horizontal resolution. An important feature of the boundary-fitted coordinate system employed here is a finer grid resolution (~5 km) in the regions of sharp topographic variations over most of the Turkish and Caucasian coasts. Another measure adopted to reduce the error is to neglect the narrow shelf regions around the basin and take the coastal boundary along ~500-m isobath in certain critical regions with slope factor exceeding 0.02. This approximation reduces the slope of the sigma surfaces and values of $(\Delta\rho/\Delta\sigma)$. Under these approximations a 2-year time

integration of the model without any forcing, initialized with the $T(z)$ and $S(z)$ profiles shown in Figure 6, produces currents of maximum intensity of 2 cm/s within the upper 100-m layer where the density variations are strongest. As the upper layer currents developed in response to the wind and thermohaline forcings are an order of magnitude stronger, we believe this effect does not cause serious concern. More importantly, as the stratification varies linearly below the pycnocline and because the pressure gradient errors vanish for linear stratification [*Mellor et al.*, 1994], the spurious currents become much weaker in the deeper levels. For example, in the layer between 200 and 500 m these currents are <1 cm/s.

Acknowledgments. This work was supported by Institute of Marine Sciences of the Middle East Technical University (Erdemli, Icel, Turkey) and by the U.S. National Science Foundation under grant INT9310226. D. Aubrey was also supported in part by funds from the Coastal Research Center of the Woods Hole Oceanographic Institution and by the U.S. Naval Research Laboratory under contract N00014-92-C-6028, modification P00006. We graciously acknowledge the technical assistance by Roberta Young, the climatological data provided by I. Gertman, and discussions with Steve Meacham and Emil Stanev on numerical modeling of the Black Sea.

References

Altman, E. N., I. F. Gertman, and Z. A. Golubeva, Climatological fields of salinity and temperature in the Black Sea, report, 109 pp., State Oceanogr. Inst., Sevastopol Branch, Sevastopol, Ukraine, 1987.

Beckmann, A., and D. B. Haidvogel, Numerical simulation of flow around a tall isolated seamount, I, Problem formulation and model accuracy, *J. Phys. Oceanogr.*, *23*, 1736–1753, 1993.

Blumberg, A. F., and H. J. Herring, Circulation modeling using orthogonal curvilinear coordinates, in *Three Dimensional Models of Marine and Estuarine Dynamics*, *Oceanogr. Ser.*, vol. 48, edited by J. C. J. Nihoul and B. M. Jamart, pp. 55–88, Elsevier, New York, 1987.

Blumberg, A. F., and G. L. Mellor, Diagnostic and prognostic numerical circulation studies of the South Atlantic Bight, *J. Geophys. Res.*, *88*, 4579–4592, 1983.

Blumberg, A. F., and G. L. Mellor, A description of a three-dimensional coastal ocean model, in *Three Dimensional Shelf Models, Coastal Estuarine Sci.*, vol. 5, edited by N. Heaps, pp. 1–16, AGU, Washington, D. C., 1987.

Boudreau, B., and P. H. Leblond, A simple evolutionary model for water and salt in the Black Sea, *Paleoceanography*, *4*(2), 157–166, 1989.

Chao, S. L., and W. Boicourt, Onset of estuarine plume, *J. Phys. Oceanogr.*, *16*, 2137–2149, 1986.

Demyshev, S. G., A numerical experiment on computations of the Black sea density fields and current velocities during summer, *Sov. J. Phys. Oceanogr.*, *3*, 293–298, 1992.

Dzhioev, T. K., and A. S. Sarkisyan, Numerical computations of the Black Sea currents, *Izv. Acad. Sci. USSR Atmos. Oceanic Phys.*, Engl. Transl., *6*, 217–223, 1976.

Eremeev, V. N., L. M. Ivanov, S. V. Kochergin, and O. V. Melnichenko, Seasonal variability and types of currents in the upper layer of the Black Sea, *Sov. J. Phys. Oceanogr.*, *3*, 193–208, 1992.

Filippov, D. M., The cold intermediate layer in the Black Sea, *Oceanology*, Engl. Transl., *5*(4), 47–52, 1965.

Gamsakhurdiya, G. R., and A. S. Sarkisyan, Diagnostic calculations of current velocities in the Black Sea, *Oceanology*, Engl. Transl., *15*, 164–167, 1976.

Gerdes, R., A primitive equation ocean circulation model using a general vertical coordinate transformation, I, Description and testing of the model, *J. Geophys. Res.*, *98*, 14,683–14,701, 1993.

Gill, A. G., Adjustment under gravity in a rotating channel, *J. Fluid Mech.*, *11*, 603–621, 1976.

Haidvogel, D. B., J. L. Wilkin, and R. E. Young, A semi-spectral primitive equation oceanic circulation model using vertical sigma and orthogonal curvilinear horizontal coordinates, *J. Comput. Phys.*, *94*, 151–185, 1991.

Haney, R. L., On the pressure gradient force over steep topography in sigma coordinate ocean models, *J. Phys. Oceanogr.*, *21*, 610–619, 1991.

Hellermann, S., and M. Rosenstein, Normal monthly wind stress over the World Ocean with error estimates, *J. Phys. Oceanogr.*, *13*, 1093–1104, 1983.

Hendershott, M. C., and P. Malanotte-Rizzoli, The winter circulation of the Adriatic Sea, *Deep Sea Res.*, *23*, 353–373, 1976.

Holland, W. R., Baroclinic and topographic influences on the transport in western boundary currents, *Geophys. Fluid Dyn.*, *4*, 187–210, 1973.

Izdar, E., and J. W. Murray, *Black Sea Oceanography*, *NATO ASI Ser., Ser. A*, 487 pp., Kluwer Academic, Norwell, Mass., 1992.

Klimok, V. I., and K. K. Makeshov, Numerical modeling of the seasonal variability of hydrophysical fields in the Black Sea, *Sov. J. Phys. Oceanogr.*, *4*, 27–33, 1993.

Latif, M. A., T. Oguz, E. Ozsoy, and U. Unluata, Observations of the Mediterranean effluent in the Black Sea, *Deep Sea Res.*, *38*, S711–S723, 1991.

Malanotte-Rizzoli, P., and A. Bergamasco, The general circulation of the Eastern Mediterranean, I, The barotropic, wind-driven circulation, *Oceanol. Acta*, *12*, 335–351, 1989.

Malanotte-Rizzoli, P., and A. Bergamasco, The wind and thermally driven circulation of the Eastern Mediterranean, II, The baroclinic case, *Dyn. Atmos. Oceans*, *15*, 355–419, 1991.

Marchuk, G. I., A. Kordzadze, and Yu. N. Skiba, Calculation of the basic hydrological fields in the Black Sea, *Izv. Acad. Sci. USSR Atmos. Oceanic Phys.*, Engl. Transl., *11*, 379–393, 1975.

McCalpin, J. D., A comparison of second-order and fourth-order pressure gradient algorithms in a σ coordinate ocean model, *Int. J. Numer. Methods Fluids*, *18*, 361–383, 1994.

Mellor, G. L., User's guide for a three dimensional, primitive equation, numerical ocean model, report, 35 pp., Program in Atmos. and Ocean. Sci., Princeton Univ., Princeton, N. J., 1991.

Mellor, G. L., and T. Ezer, A Gulf Stream model and an altimeter assimilation scheme, *J. Geophys. Res.*, *96*, 8779–8795, 1991.

Mellor, G. L., and T. Yamada, Development of a turbulence closure model for geophysical fluid problems, *Rev. Geophys.*, *20*, 851–875, 1982.

Mellor, G. L., T. Ezer, and L. Y. Oey, The pressure gradient conundrum of sigma coordinate ocean models, *J. Atmos. Oceanic Technol.*, *11*, 1–9, 1994.

Moskalenko, L. V., Calculation of stationary wind-driven currents in the Black Sea, *Oceanology*, Engl. Transl., *15*, 168–171, 1976.

Murray, J. W., Black Sea oceanography: Results from the 1988 Black Sea expedition, *Deep Sea Res., Part A*, *38*, suppl. 2, 1266 pp., 1991.

Murray, J. W., Z. Top, and E. Ozsoy, Hydrographic properties and ventilation of the Black Sea, *Deep Sea Res., Part A*, *38*, suppl. 2, S663–S690, 1991.

National Center for Atmospheric Research, *NCAR Graphics User's Guide*, Scientific Computing Division, Boulder, Colo., 1987.

Oey, L. Y., G. L. Mellor, and R. I. Hires, A three dimensional simulation of the Hudson-Raritan estuary, I, Description of the model and model simulations, *J. Phys. Oceanogr.*, *15*, 1676–1692, 1985.

Oguz, T., and L. Rozman, Characteristics of the Mediterranean underflow in the southwestern Black Sea continental shelf/slope region, *Oceanol. Acta*, *14*, 433–444, 1991.

Oguz, T., M. A. Latif, H. I. Sur, E. Ozsoy, and U. Unluata, On the dynamics of the southern Black Sea, in *The Black Sea Oceanography*, *NATO ASI Ser., Ser. A*, edited by E. Izdar and J. W. Murray, pp. 43–64, Kluwer Academic, Norwell, Mass., 1991.

Oguz, T., P. E. La Violette, and U. Unluata, The Black Sea circulation: Its variability as inferred from hydrographic and satellite observations, *J. Geophys. Res.*, *97*, 12,569–12,584, 1992.

Oguz, T., V. S. Latun, M. A. Latif, V. V. Vladimirov, H. I. Sur, A. A. Markov, E. Ozsoy, B. B. Kotovshchikov, V. V. Eremeev, and U. Unluata, Circulation in the surface and intermediate layers of the Black Sea, *Deep Sea Res., Part I*, *40*, 1597–1612, 1993.

Oguz, T., et al., Mesoscale circulation and thermohaline structure of

the Black Sea observed during HydroBlack '91, *Deep Sea Res., Part I, 41*, 603–628, 1994.
Oguz, T., D. Aubrey, S. Besiktepe, L. Ivanov, V. Diacanu, and U. Unluata, On the ADCP observations of the western Black Sea Rim Current, *Deep Sea Res., Part I*, in press, 1995.
Ovchinnikov, I. M., and Yu. I. Popov, Evolution of the cold intermediate layer in the Black Sea, *Oceanology*, Engl. Transl., *27*, 555–560, 1987.
Ozsoy, E., Z. Top, and U. Unluata, The evolution of Mediterranean water in the Black Sea: Interior mixing and material transport by double diffusive intrusions, *Prog. Oceanogr., 31*, 275–320, 1994.
Shaw, P. T., and G. T. Csanady, Self-advection of density perturbations on a sloping continental shelf, *J. Phys. Oceanogr., 13*, 769–782, 1983.
Simonov, A. I., and E. N. Altman, *Gidrometeorologiaya i Gidrokhimiya Mareij SSSR*, vol. 1, Chernoe More, Sevastopol, Ukraine, 1991.
Stanev, E. V., On the mechanisms of the Black Sea circulation, *Earth Sci. Rev., 28*, 285–319, 1990.
Stanev, E., D. I. Trukhchev, and V. M. Roussenov, *The Black Sea Circulation and Numerical Modeling of the Black Sea Currents*, (in Russian), 222 pp., Sofia University Press, Sofia, Bulgaria, 1988.
Stanev, E. V., V. M. Roussenov, N. H. Rachev, and J. V. Staneva, Sea response to atmospheric variability: Model study for the Black Sea, *J. Mar. Syst.*, in press, 1995.
Staneva, J. V., Heat balance of the Black Sea, M.Sc. thesis, 85 pp., Sofia Univ., Sofia, Bulgaria, 1993.
Sur, H. I., E. Ozsoy, and U. Unluata, Boundary current instabilities, upwelling, shelf mixing and eutrophication processes in the Black Sea, *Prog. Oceanogr.*, in press, 1995.
Tolmazin, D., Changing coastal oceanography of the Black Sea, I, Northwestern Shelf, *Prog. Oceanogr., 15*, 217–276, 1985a.
Tolmazin, D., Changing coastal oceanography of the Black Sea, II, Mediterranean effluent, *Prog. Oceanogr., 15*, 277–316, 1985b.
Trukhchev, D. I., and Y. L. Demin, The Black Sea general circulation and climatic temperature and salinity fields, *ComsBlack 92-010 Tech. Rep., Publ. WHOI-92-34*, Woods Hole Oceanogr. Inst., Woods Hole, Mass., 1992.
Unluata, U., T. Oguz, M. A. Latif, and E. Ozsoy, On the physical oceanography of the Turkish Straits, in *The Physical Oceanography of Sea Straits, NATO ASI Ser., Ser. C*, edited by J. Pratt, pp. 25–60, Kluwer Academic, Norwell, Mass., 1989.
Vennell, R. M., and P. Malanotte-Rizzoli, The influence of a steady baroclinic deep ocean on the shelf: The vertically well-mixed case, *J. Phys. Oceanogr., 20*, 489–505, 1990.
Wang, D. P., The strait surface outflow, *J. Geophys. Res., 92*, 10,807–10,825, 1987.
Whitehead, J. A., A laboratory study of gyres and uplift near the Strait of Gibraltar, *J. Geophys. Res., 90*, 7045–7060, 1985.
Whitehead, J. A., and A. R. Miller, Laboratory simulation of the gyre in the Alboran Sea, *J. Geophys. Res., 84*, 3733–3742, 1979.
Yuce, H., Investigation of the Mediterranean water in the Strait of Istanbul (Bosphorus) and the Black Sea, *Oceanol. Acta, 13*, 177–186, 1990.
Zavatarelli, M., and G. L. Mellor, The numerical study of the Mediterranean Sea circulation, *J. Phys. Oceanogr.*, in press, 1995.

D. Aubrey, Department of Geology and Geophysics, Woods Hole Oceanographic Institution, Woods Hole, MA 02543. (e-mail: aubrey@mvd. whoi.edu)
P. Malanotte-Rizzoli, Department of Earth, Atmospheric and Planetary Sciences, Massachusetts Institute of Technology, Cambridge, MA 02139. (e-mail: rizzoli@ocean.mit.edu)
T. Oguz, Institute of Marine Sciences, Middle East Technical University, P. O. Box 28, Erdemli, 33761, Icel, Turkey. (e-mail: aguz@deniz.ims.metu.edu.tr)

(Received September 5, 1994; revised November 28, 1994; accepted January 3, 1995.)